# Ram pressure shaping HVC droplets

# FAST HI observations of HVC AC-III and theoretical interpretation

Xunchuan Liu (刘训川)<sup>1\*</sup>

Leiden Observatory, Leiden University, P.O. Box 9513, 2300RA Leiden, The Netherlands

Received xxx xx

#### **ABSTRACT**

FAST H1 observations reveal unprecedented internal structures of the high-velocity cloud AC-III, which is found to consist of several coherent subclumps (D1-D6) with nearly constant line widths of ~ 20 km s<sup>-1</sup>, while the global velocity spread ranges from -220 to -180 km s<sup>-1</sup>. These subclumps exhibit parabolic morphologies, consistent with ram-pressure-confined droplets, with their heads tending to point toward the Galactic plane. A steady-state model reproduces both the morphology and the observed exponential density profiles. The tip density reaches  $\sim 2 \text{ cm}^{-3}$ , implying an ambient medium density of  $\sim 10^{-3} \text{ cm}^{-3}$ , in agreement with the Galactic warm ionized medium at a distance of ~ 5 kpc. Deviations from symmetric droplet shapes, along with internal patterns such as strip-like ridges, rings, and holes, indicate rich internal dynamics. In particular, the observations are consistent with fluid loops forming inside the droplets in response to interactions between neighboring subclumps. These loops can generate ring-like dynamic patterns and drive secondary turbulence, sustaining long-lived internal motions. An intermediate-velocity component (-150 to -100 km s<sup>-1</sup>) exhibits a shell-like morphology aligned with the head of AC-III, possibly shaped by pressure interactions mediated by the WIM. Overall, we suggest that HVC AC-III is entering the Galactic WIM layer and being sculpted by ram pressure into a droplet-like morphology, providing a valuable case for studying the structure formation, turbulence origin, and dynamic evolution of

Key words. ISM: kinematics and dynamics — ISM: structure — ISM: individual objects (HVC AC-III) — Galaxy: halo — radio

Received xxx xx

ABST

FAST H i observations reveal unprecedented internal structures of coherent subclumps (D1–D6) with nearly constant line widths of to –180 km s<sup>-1</sup>. These subclumps exhibit parabolic morphologies tending to point toward the Galactic plane. A steady-state mode density profiles. The tip density reaches ~ 2 cm<sup>-3</sup>, implying an Galactic warm ionized medium at a distance of ~ 5 kpc. Deviat such as strip-like ridges, rings, and holes, indicate rich internal oloops forming inside the droplets in response to interactions bet dynamic patterns and drive secondary turbulence, sustaining long-to –100 km s<sup>-1</sup>) exhibits a shell-like morphology aligned with the by the WIM. Overall, we suggest that HVC AC-III is entering the droplet-like morphology, providing a valuable case for studying the HVCs, as well as the physical properties of the ambient medium.

Key words. ISM: kinematics and dynamics — ISM: structure — lines: ISM (HI)

1. Introduction

High-velocity clouds (HVCs) are H1 structures moving at velocities inconsistent with Galactic rotation (Wakker 1991; Westmeier 2018). Absorption-line studies toward halo stars behind a limited sample of HVCs detect associated ionized gas, indicating that they are multi-phase systems typically located several kiloparsecs (kpc) above the Galactic plane (e.g., van Woerden et al. 1999; Wakker et al. 2008; Thom et al. 2008; Peek et al. 2016). This ionized gas may arise both from the ionization balance intrinsic to the HVC itself and from the accumulation and heating of ambient material during interactions with the hot halo and the Galactic layer of the warm ionized medium (WIM). The predominantly negative velocities of HVCs (Wakker 1991; Wakker et al. 2008; Westmeier 2018) indicate that they may trace the infall of low-metallicity gas from the circumgalactic medium onto the Galactic disk (Bregman 1980; de Boer 2004; Fox et al. 2016; Cashman et al. 2023). Therefore, HVCs are widely recognized as key components of the Galactic gas cycle, playing a crucial Cashman et al. 2023). Therefore, HVCs are widely recognized as key components of the Galactic gas cycle, playing a crucial role in feeding the Milky Way with fresh material, sustaining star formation, and mediating the exchange of gas between the disk and the halo. However, there is still no consensus on their specific origins or evolutionary sequence.

Another important characteristic of HVCs is that, thanks to the improved resolutions of modern single-dish telescopes and interferometric arrays, their internal structures are revealed to be far more complex than previously anticipated. Highresolution observations show that some HVCs exhibit filamentary morphologies, often appearing as elongated or striplike structures aligned with the large-scale features of infalling streams (Lockman et al. 2008; Blagrave et al. 2017; Holm-Hansen et al. 2024, 2025). Recent FAST observations of the very-high-velocity cloud (VHVC) G165, a subset of HVCs with  $|V_{\rm LSR}| \gtrsim 200 \ {\rm km \ s^{-1}}$ , reveal intricate internal structures, consisting of intertwined filaments forming a complex, network-like pattern produced by turbulent compression, the origin of which remains unclear (Liu et al. 2025a). This dynamic morphological complexity points to rich internal processes that may arise from the interplay between turbulence, thermal instability, and environmental interactions.

A natural expectation is that the infalling nature of HVCs, combined with their interactions with the diverse ambient environment during infall, provides a framework for their evolutionary sequence, shaping their global morphology, internal turbulence, dynamic structures, and multi-phase transitions. To explore this scenario, it is important to examine the dynamic patterns induced by interactions between HVCs and the surrounding gas. Most HVCs, however, do not display morphologies clearly shaped by pressure interactions (e.g., Westmeier 2018). This can be attributed to the high temperature ( $\sim 10^6$  K) of the hot halo (Shapiro & Field 1976; Bregman 1980; Barone et al. 2024), where HVCs move largely unaffected, experiencing subsonic or subthermal motion relative to the ambient halo gas. This picture may change dramatically when HVCs enter the probable cold component of the hot halo (e.g., Barone et al. 2024), or more likely, the much colder ( $10^4$  K) and denser ( $10^{-3}$  cm<sup>-3</sup>) Galactic layer of the WIM, which has a compact, disk-like structure

<sup>\*</sup> liuxunchuan001@gmail.com

compared to the hot halo and is constrained by the Galactic gravitational potential and magnetic field (Reynolds 1991; Gaensler et al. 2008; Haffner et al. 2009). In this environment, interactions are expected to strongly influence both the morphology and internal structure of HVCs.

We examined the HVCs revealed by the all-sky H<sub>I</sub> survey HI4PI (HI4PI Collaboration et al. 2016; Westmeier 2018) and found that AC-III exhibits a head-tail morphology shaped by ram pressure, with the head pointing toward the Galactic plane. AC-III is located at  $(l,b) = (190^{\circ}, -30^{\circ})$ , with a radial velocity of  $\sim -200$  km s<sup>-1</sup>. The head has an angular size of  $\sim 2^{\circ}$ , oriented toward the Galactic plane, suggesting that this system is intrinsically approaching us at very high velocity, rather than its apparent motion being a projection effect. AC-III therefore provides an excellent case to study interactions with the ambient environment; however, the limited resolution of HI4PI (beam size > 10') makes it difficult to investigate its internal structures in sufficient detail to place effective constraints on these interactions. This motivated us to observe AC-III using FAST, providing an angular resolution of  $\sim 3'$ .

In this work, we reveal the droplet-like substructures of AC-III resolved by FAST observations and provide a theoretical interpretation of its morphology and internal density patterns within the framework of ram-pressure-induced droplets and their inter-droplet interactions. The paper is structured as follows. Sect. 2 describes the FAST observations and data processing. Sect. 3 presents the observed morphology and kinematics of AC-III. In Sect. 4, we introduce the steady-state droplet morphology and examine the effects of projection on the observed shapes and density profiles. Sect. 5 investigates how local interactions cause deviations from symmetric droplet morphologies, producing internal strip-like and ring-like dynamic patterns inspired by the observations. Sect. 6 discusses the properties of the ambient gas inferred from droplet fitting and explores possible interactions between the HVC and lower-velocity gas in the AC-III region. Finally, Sect. 7 summarizes the main findings and conclusions.

#### 2. Observations and data reduction

#### 2.1. AC-III

At the Galactic anti-center ( $l \sim 180^\circ$ ), HVC components are dominated by Chain A, the AC group, and the Cohen Stream (Westmeier 2018). Chain A, the AC shell, AC-I/II, and the Cohen Stream are all extended or elongated structures spanning several tens of degrees. AC-III is a more compact clump, with an angular size of a few degrees (Figure 1), located between AC-I/II and the Cohen Stream, and its distance remains poorly constrained. Tamanaha (1996) suggested that the AC shell lies within  $\sim 6.5$  kpc from the Sun, while Wakker et al. (2008) estimated a distance bracket of 5.0–11.7 kpc for the Cohen Stream. Chain A is measured to be within 10 kpc (van Woerden et al. 1999). These estimates imply that HVCs in the anti-center sky are relatively nearby and likely associated with the Galactic disk–halo interface. For the purposes of this work, we adopt a distance of 5 kpc for AC-III.

#### 2.2. FAST observations

We conducted FAST (Nan et al. 2011) observations of the high-velocity cloud AC-III (FAST project ID PT2025\_0043, PI: Xunchuan Liu) between 2025 August 12 and 15. The data were obtained in on-the-fly (OTF) mode with the *L*-band 19-beam

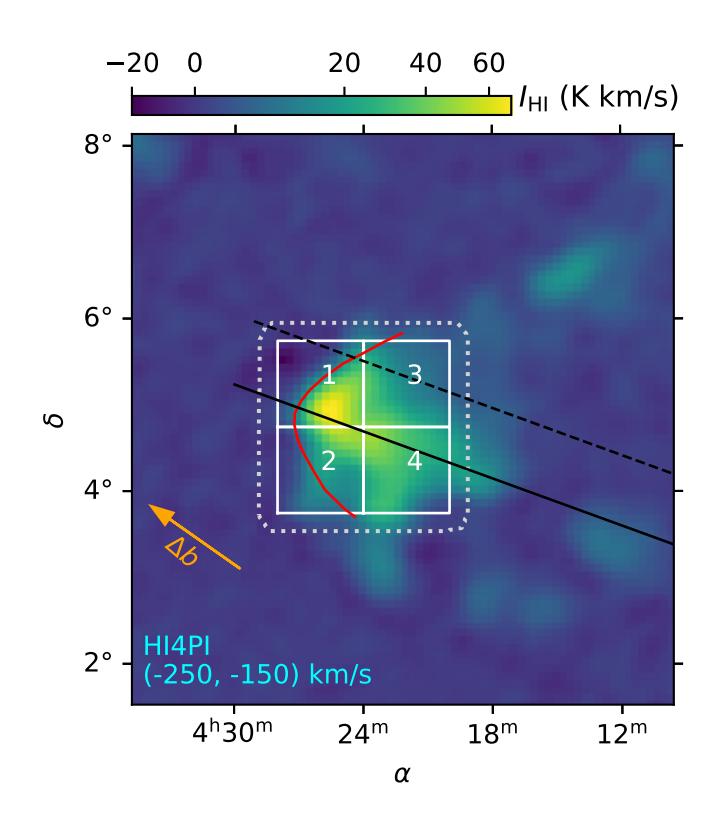


**Fig. 1.** HI4PI (HI4PI Collaboration et al. 2016) moment-0 map of AC-III, integrated over -250 to -150 km s<sup>-1</sup>. White squares indicate the four OTF fields observed with FAST (see Sect. 2). The dotted white line outlines the full FAST coverage, including the noisy margins (see the upper-left panel of Fig. A.2). The red line traces the global trend of the ram-pressure–induced parabolic front, identified from a joint analysis of the HI4PI and FAST images. The field center of the white dashed box (FAST sky coverage) has Galactic coordinates  $(\ell, b) = (189.445^{\circ}, -29.636^{\circ})$ . The orange arrow denotes the direction of increasing Galactic latitude,  $\Delta b$ , i.e., toward the Galactic plane, since the target lies in the southern Galactic hemisphere. The black solid and dashed lines indicate two position–velocity cuts, labeled PV1 and PV2, respectively, used for the analysis presented in Sect. 6.3.

receiver. The declination of the target ( $\sim 5^{\circ}$ ) enables the observations to be performed within FAST's optimal zenith angle range ( $\theta_{ZA} < 26.4^{\circ}$ ), where the illuminated aperture reaches 300 m(Jiang et al. 2019).

The L-band front end provides full-polarization measurements: the auto-correlations XX and YY, together with the real and imaginary parts of the cross-correlations XY. In this work, we focus on Stokes I, obtained by averaging the two autocorrelations (XX and YY). The system has a typical FWHM beam size of  $\sim 3'$  at 1.4 GHz, a system temperature below 24 K, and a beam efficiency of 0.85 for extended sources (Jiang et al. 2019; Liu et al. 2022). The telescope operated with a tracking accuracy of 0.2'. The spectral backend records full polarization and provides 1024k spectral channels over a bandwidth of 500 MHz (from 1 to 1.5 GHz), resulting in a frequency resolution of  $\delta f \sim 0.48$  kHz per channel, corresponding to a velocity resolution of  $\sim 0.1~\text{km s}^{-1}$  at 1.42 GHz. Spectra from the backend are recorded every  $dt_{\text{sample}} = 240 \times t_{\text{period},0} \sim 0.5033 \text{ s}$ , where  $t_{\rm period,0} = 2^{21} \text{ ns} \sim 0.00209 \text{ s}$  is the time interval of an individual FFT of the backend. Knowing the accurate sampling time is important, as the data reduction depends on precise mapping from spectral index to time and then to sky coordinates (Liu et al. 2025b).

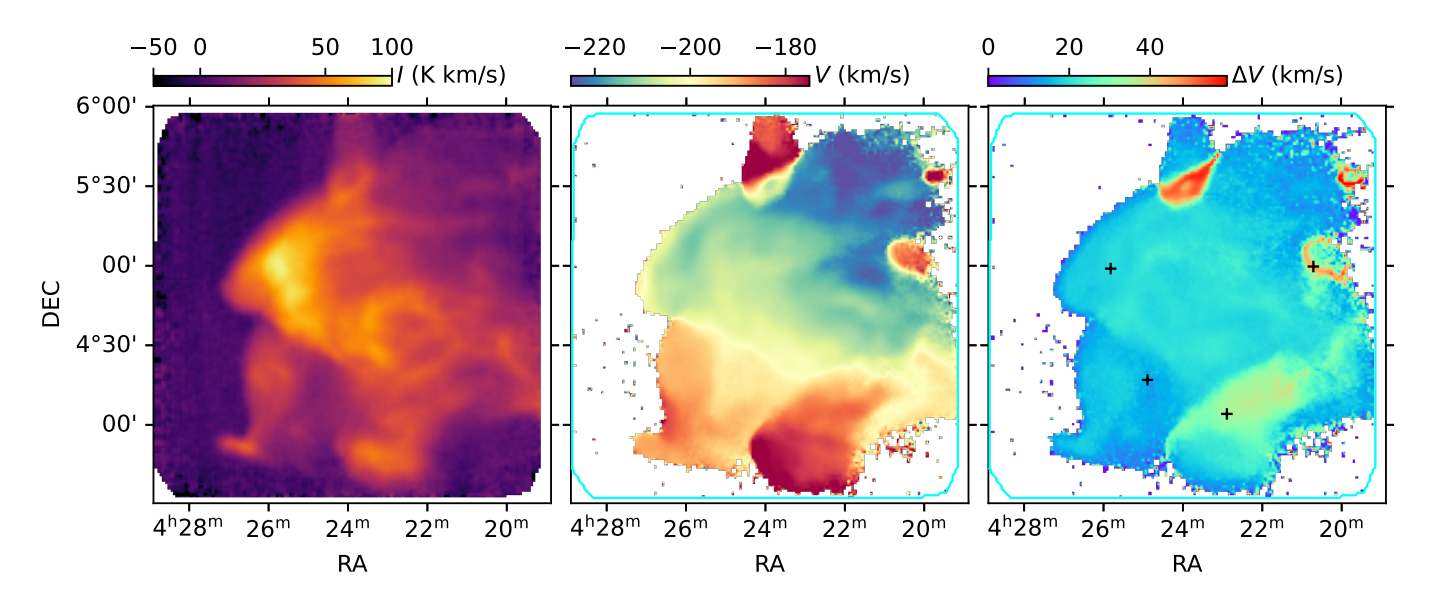
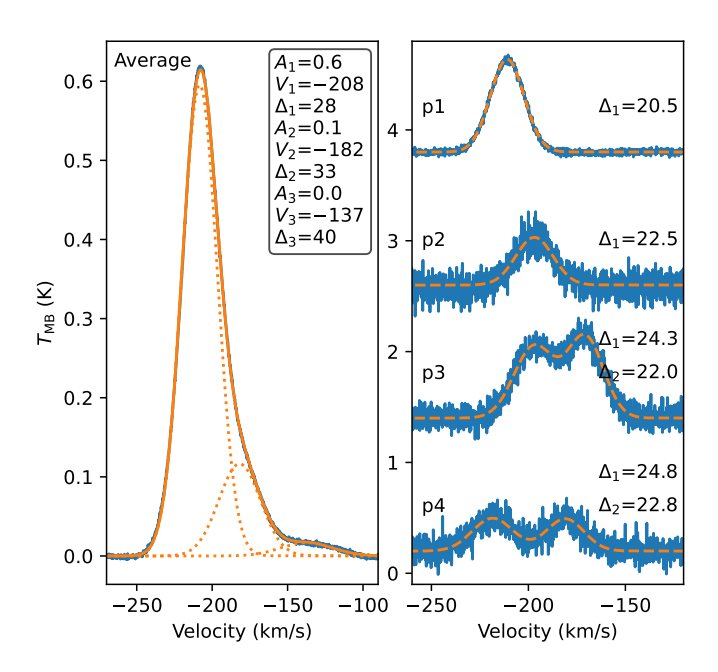


Fig. 2. Moment maps of the FAST H<sub>I</sub> emission of AC-III, integrated over -250 to -160 km s<sup>-1</sup>. The moment 0 map ( $M_0$  or I, left) is shown without thresholding, while the velocity ( $M_1$  or V, middle) and line-width ( $\Delta V$ , Eq. 2, right) maps use only channels above  $3.5\sigma$ . The cyan outline in the middle and right panels marks the FAST coverage (Figure 1). Spectra at the four black crosses in the right panel, labeled p1-p4 from left to right, are shown in Figure 3.



**Fig. 3.** Left: Mean spectrum (blue) of the FAST-covered region of AC-III, together with a three-component Gaussian fit (orange). The Gaussian fitting results are shown in the upper right corner, including the peak brightness temperature ( $T_{\rm peak}$ ), the central velocity (V), and the FWHM line width ( $\Delta$ ) of each component. Right: Same as the left panel but for the spectra at positions p1–p4 (see right panel of Figure 2). The fitted FWHM line widths are labeled. For clarity, the spectrum at p1 has been divided by a factor of five.

AC-III was covered with four square-shape fields (Figure 1), each measuring  $1^{\circ} \times 1^{\circ}$ . To satisfy Nyquist sampling within each scanning row, the feed cabin was rotated clockwise by 53.4° (see Liu et al. 2025b for the scanning pattern). The mapping was performed with scans along declination at a speed of 30'' s<sup>-1</sup>, with successive rows separated along right ascension by 1.7'. The redundant sampling improves sensitivity and suppresses strip-

ing caused by possible differences in the response of individual beams. To cover each field, 36 rows were scanned. With a 54 s turnaround time ( $t_{\text{return}}$ ) for each row, 6210 s of telescope time were required per field (not including an additional 10-minute overhead). In total, 8 hours of telescope time were used to cover the four fields.

For calibration, the low-noise mode of the temperature-stabilized noise diode ( $T_{\rm cal} \sim 1.1~{\rm K}$ ) was used. Modulated noise was injected every 2 s (more precisely, every  $4\,dt_{\rm sample}$ ) with equal on/off intervals, and each noise injection lasted for  $2\,dt_{\rm sample}$ , synchronized with the spectral backend.

### 2.3. Data reduction

The data reduction process—including gridding, Doppler correction, calibration, spectral baseline subtraction for each field, and merging the data cubes of different fields into a single cube—follows the procedures described in Liu et al. 2025b. During the observations, strong RFI occasionally occurred in short intervals of about 1 minute. The affected data were removed as described in Sect. A.

#### 3. Observational results of HVC AC-III

Denote  $M_n$  as the  $n_{\text{th}}$ -order moment of a spectrum T(v), defined by

$$M_n = \frac{\int (v - v_0)^n T(v) \, dv}{\int T(v) \, dv},\tag{1}$$

where  $v_0 = 0$  for n = 1, and  $v_0 = M_1$  for n > 1.  $M_0$  and  $M_1$  correspond to the integrated intensity (I) and the mean velocity (V) of the spectrum, respectively. The  $M_2$ -derived line width can then be estimated as

$$\Delta V = \sqrt{8 \ln 2 M_2}.\tag{2}$$

Figure 2 shows the moment maps  $(I, V, \text{ and } \Delta V)$  of the H<sub>I</sub> emission in AC-III, observed with FAST, within the velocity range -250 to -160 km s<sup>-1</sup>.

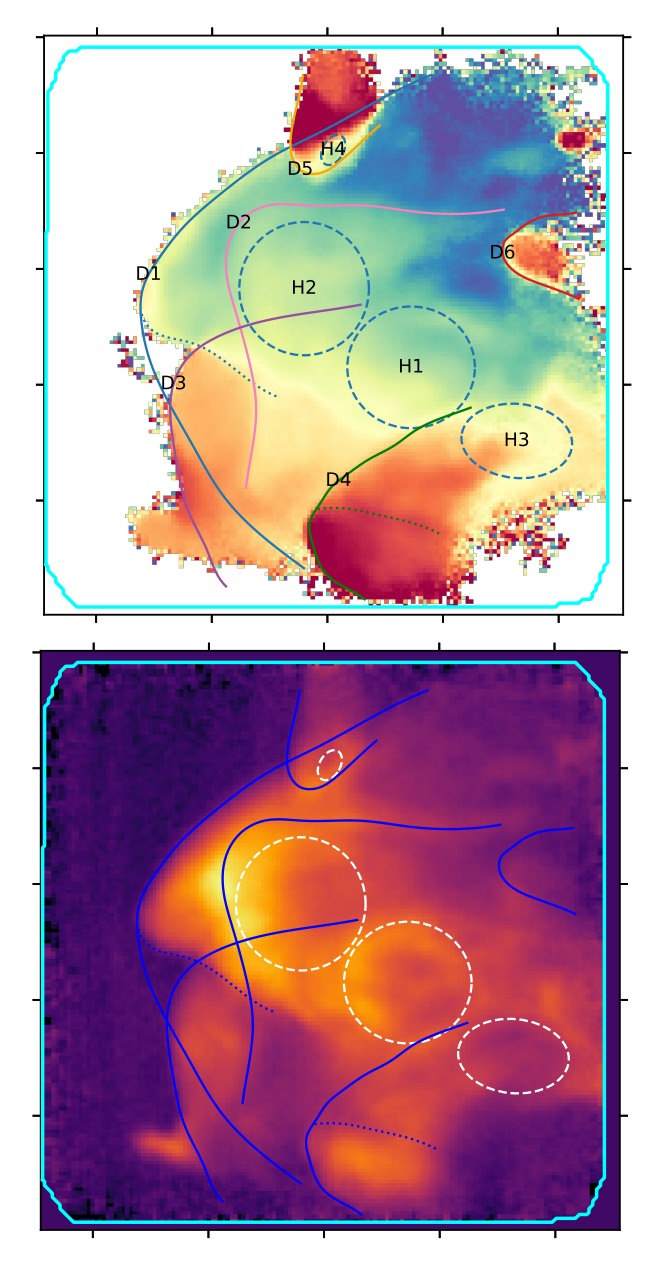


**Fig. 4.** Moment 0 and 1 maps, similar to those in Figure 2, with curves highlighting droplet-like features and ellipses indicating ring-like (or hole-like) structures. The colorbars and coordinate ticks are the same as in the corresponding panels of Figure 2 and are therefore not labeled. The blue curve (D1) in the upper panel corresponds to the red curve in Figure 1.

The average spectrum of AC-III within the FAST-covered region can be decomposed into three Gaussian components (Figure 3). The velocity range adopted in Figure 2 corresponds to the two major components, while a third, relatively weak component appears intermittently in the range  $v \sim -150$  to -100 km s<sup>-1</sup>. Below, we focus on the two major components. The nature of the weak component—whether it represents a distinct intermediate-velocity cloud (IVC) or is dynamically associated with AC-III—will be discussed in Sect. 1.

#### 3.1. Subclumps in constant line widths

The H<sub>I</sub> spectra exhibit well-defined Gaussian profiles with typical line widths of  $\sim 20 \text{ km s}^{-1}$ . At positions where the  $M_2$ -

derived line width is large, the spectra can be decomposed into two Gaussian components, each with  $\Delta V \sim 20~\rm km~s^{-1}$  (see Figure 3 for example). Even in pixels where  $M_2$  gives narrower widths (e.g., p2 in Figure 2), Gaussian fitting still recovers  $\Delta V \sim 20~\rm km~s^{-1}$ . This shows that the reduced  $M_2$  values are not intrinsic, but result from low-intensity spectra with masked Gaussian wings.

These results indicate that AC-III can be described as multiple subclumps (we call them droplets in Sect. 3.2 according to their morhpology), each characterized by a nearly constant Gaussian line width of  $\sim 20~\rm km~s^{-1}$ . The broader global velocity distribution of AC-III, spanning  $-220~\rm to~-180~km~s^{-1}$  (middle panel of Figure 2), is produced by clump-to-clump motions among these subclumps.

When the H<sub>I</sub> spectrum is optically thin—which is always the case for HVCs owing to their low gas density—the conversion between the integrated intensity and the H<sub>I</sub> column density is given by (Li & Goldsmith 2003; McClure-Griffiths et al. 2023):

$$N(\text{H I}) = 1.84 \times 10^{18} \frac{I_{\text{HI}}}{\text{K km s}^{-1}} \text{ cm}^{-2}.$$
 (3)

For a single Gaussian line profile,  $I_{\rm HI}=1.064\,T_{\rm peak}\,\Delta V$ , where  $T_{\rm peak}$  is the peak brightness temperature. Thus, for  $\Delta V=20\,{\rm km\,s^{-1}}$ ,

$$N({\rm H\,I}) \approx 3.9 \times 10^{19} \left(\frac{T_{\rm peak}}{{\rm K}}\right) {\rm cm}^{-2}.$$
 (4)

The peak brightness temperature, averaged over  $1^{\circ}$  (the typical angular scale of the subclumps), is  $\sim 1$  K. The corresponding volume density is then

$$n \sim \frac{N(\text{H I})}{d \times 1^{\circ}} \sim 0.2 \, d_5^{-1} \, \text{cm}^{-3},$$
 (5)

where d is the distance and  $d_5$  is d in units of 5 kpc. The total flux (F) of the covered region is 75 K km s<sup>-1</sup> deg<sup>2</sup>, corresponding to a total mass of

$$M_{\text{tot}} \sim 8.5 \times 10^3 \, d_5^2 \, M_{\odot}.$$
 (6)

Assuming a velocity dispersion  $\sigma_{\nu} = 10 \text{ km s}^{-1}$  and an angular radius of 1°, the virial mass is

$$M_{\rm vir} = \frac{R\sigma_{\nu}^2}{G} \sim 2 \times 10^6 \ d_5 \ M_{\odot}. \tag{7}$$

Additional contributions from turbulence and clump-to-clump motions would further increase  $M_{\rm vir}$ . Thus,  $M_{\rm vir} \gg M_{\rm tot}$  for any reasonable distance, indicating that self-gravity can be safely neglected.

The line width and density are comparable to those of the typical warm neutral medium (WNM), indicating that WNM dominates the neutral component of HVC-III. The nearly uniform  $\Delta V \sim 20~{\rm km~s^{-1}}$  strongly suggests that each subclump in AC-III is a coherent parcel of transonic or subsonic WNM, with most of the dynamical energy stored in clump-to-clump motions.

#### 3.2. Subclumps as droplets

The moment 0 maps can be decomposed into a number of subclumps whose boundaries are approximately parabolic in shape. These subclumps are even more clearly delineated in the moment 1 maps, where their parabolic heads are especially prominent. The column density is typically enhanced in the head region and decreases rapidly toward the broader tail. We interpret these features as droplets formed under external pressure

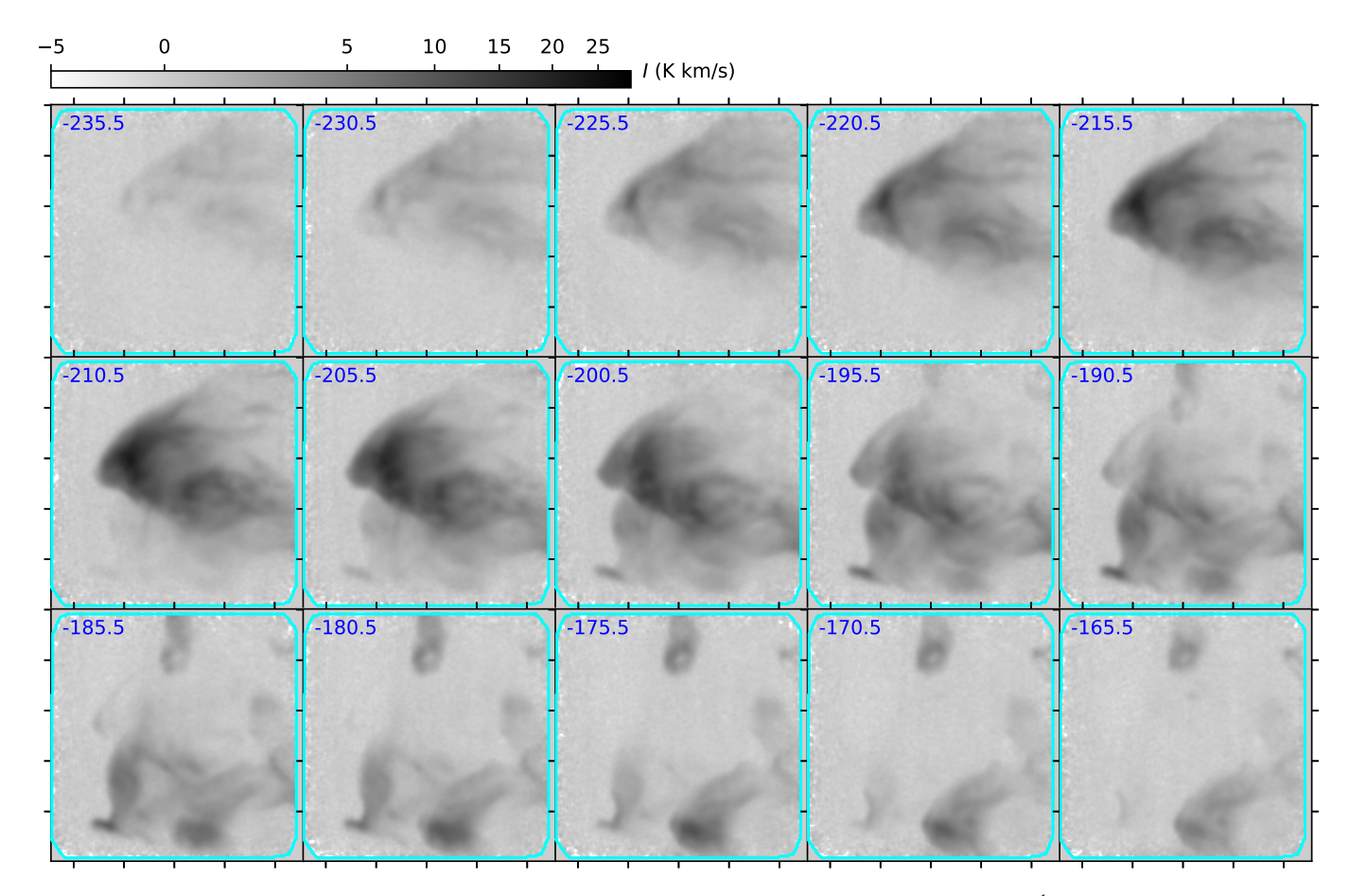


**Fig. 5.** Channel maps of the H<sub>I</sub> emission of AC III observed with FAST. Each panel is integrated over 5 km s<sup>-1</sup>, with consecutive panels offset by the same velocity step. The central velocity of each interval (in km s<sup>-1</sup>) is indicated by blue text in the upper-left corner of each panel. All panels share the same colorbar. The coordinate ticks are identical to those in Figure 2, and the cyan line outlines the region covered by the FAST observations.

(Sect. 4). In total, six such droplets are identified and labeled D1 through D6 (Figure 4). Throughout this work, unless otherwise noted, references to cardinal directions are given in Galactic coordinates. For AC-III, north points toward the Galactic plane, and west points in the direction of Galactic rotation.

To constrain the global motion of AC-III, we examined the orientations of the droplet heads (Figure 4), which show modest variations but are overall biased toward the Galactic plane. The negative velocities of AC-III cannot be explained by Galactic rotation because of its anti-center location at  $l \sim 190^\circ$ . Assuming a Solar rotation speed of 220 km s<sup>-1</sup> around the Galactic center and negligible orbital motion of the target, the maximum possible line-of-sight contribution from Galactic rotation is

$$v_{\text{rot,LOS}} = 220 \sin(10^{\circ}) \sim 38 \text{ km s}^{-1},$$
 (8)

which is far smaller than the observed velocity of AC-III,  $\sim$  -200 km s<sup>-1</sup>. Moreover, Eq. 8 predicts a positive (receding) velocity, in contrast to the observed negative (approaching) value. We therefore conclude that AC-III is intrinsically moving toward us. Combined with this intrinsic motion, the orientations of the droplets suggest that they are shaped by ram pressure during infall into the Galaxy. In this scenario, the deceleration force associated with ram pressure naturally compresses the gas into the head region (Sect. 4.2).

Further examination of the droplets reveals that in several cases their projected boundaries overlap (Figure 4). The most prominent structure is droplet D1, with an angular size of  $\sim 2^{\circ}$ ,

whose head points toward the Galactic north with a slight shift toward the east. Droplets D3 and D4 are fainter but comparable in size ( $\sim 1^{\circ}$ ) and are located along the eastern boundary of D1. In contrast, D5 and D6 are more compact, each  $\sim 0.2^{\circ}$  across, situated at the western boundary and at the tail of D1, respectively. D3–D6 exhibit velocities more than 20 km s<sup>-1</sup> redder than D1 (see also the channel map in Figure 5). Droplet D2 shows a head embedded within the projected extent of D1 and a tail elongated beyond the standard parabolic form, with its eastern side extending toward D3. The  $M_2$ -derived line widths are generally enhanced at the apparent overlap regions of neighboring droplets (Figure 2). Such broadening, however, does not by itself imply interaction, since line-of-sight overlap can produce similar effects. Additional evidence is needed to determine whether the droplets are dynamically interacting.

The morphology of D1 reveals deviations from a purely rampressure—shaped steady state. Its head is distorted relative to the ideal parabolic shape, with the eastern boundary compressed inward compared to the smoother and more rounded western side. In Figure 4, this eastern boundary (blue curve in the upper panel) is extrapolated based on: (1) symmetry with respect to the western boundary; (2) the global morphology of AC-III as revealed by HI4PI (Figure 1); and (3) alignment with the eastern boundaries of D2, D3, and D4. As the major component of AC-III, D1 is expected to play a primary role in resisting ram pressure, with its shape largely governing the overall morphology of the system. The western boundaries of D3 and D4 intrude into the pro-

jected extent of D1. For D3, the morphology in the overlapped region is difficult to disentangle, whereas for D4, the deviation from a standard droplet shape is clearly visible in the moment 1 map.

Because a droplet in steady state under ram pressure is expected to remain symmetric perpendicular to its main axis, the observed distortions are unlikely to result from ram pressure alone. The apparent intrusion of neighboring droplets, together with these departures from axial symmetry, therefore suggests that inter-droplet interactions may be occurring. Overall, these morphologies and spatial associations indicate that droplets are shaped jointly by ram pressure and possible inter-droplet compression, creating a dynamically enriched environment that may drive the internal patterns observed within the droplets (Sect. 3.3).

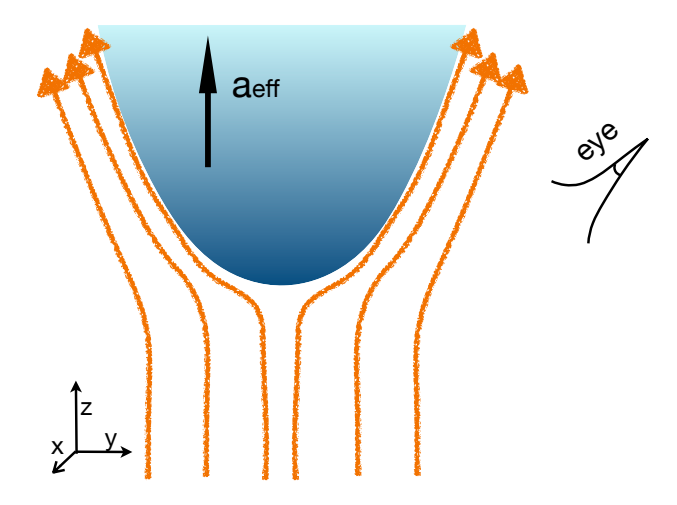
#### 3.3. Dynamic patterns: strips, rings, and holes in droplets

The higher resolution of FAST, compared to previous surveys such as HI4PI, allows us to resolve not only the parabolic morphology of the droplets but also their clear internal density patterns. These patterns, including strips, rings, and holes, provide new insights into the dynamical processes operating within the droplets.

Unlike VHVC G165, which harbors a web-like filamentary network, AC-III exhibits relatively simpler filamentary structures. These appear more like strips, preferentially oriented along the main axes of the droplets (Figure 5), suggesting that the internal density pattern is influenced by the external ram pressure. However, a perfect droplet in steady state would not display such internal structures. Their presence indicates that internal dynamics must also play a role, consistent with the observed velocity gradients both along and perpendicular to the main axes of the droplets (Figure 4).

Besides the strips, another notable internal density pattern is the presence of rings and holes. Along the eastern boundary of D1, three holes (H1–H3) with diameters of  $\sim 0.5^{\circ}$  are visible, each outlined by enhanced edges that form ring-like structures. Among them, H2 is the most typical case, showing the roundest shape. The three rings are roughly aligned along the main axis of D2, suggesting that D2 may not be an external droplet like D3 and D4, but rather a dynamical structure intrinsically embedded within D1. This interpretation is further supported by the absence of any significant line-width enhancement associated with D2. A smaller feature (H4), with a diameter of about 8′, is also seen in the overlap region between D1 and D5. Taken together, these findings suggest that rings and holes may represent a common internal pattern arising from anisotropic interactions between neighboring droplets.

In the following two sections, we develop a theoretical framework to explain how droplet morphologies are established and how they deviate from ideal forms. In Sect. 4, we derive the steady-state solution for a droplet shaped by ram pressure, assuming a static density distribution. In Sect. 5, we show that more anisotropic external pressure cannot be balanced by a steady-state density distribution and must instead induce a dynamical solution within the droplets. In this scenario, the internal velocity can remain time-independent, allowing the resulting density structure to form a stable pattern that persists over long periods.



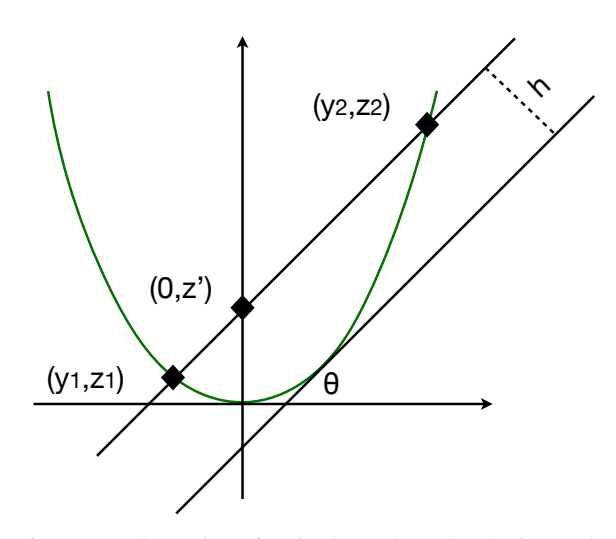


**Fig. 6.** Upper: Illustration of an isothermal gas droplet in steady state (blue, with color depth representing density), confined by ram pressure from the surrounding flows (orange arrows; Sect. 4.2). Lower: Projection of the droplet at an inclination angle  $\theta$  (Sect. 4.3), where  $\theta=0$  corresponds to a line of sight perpendicular to the droplet axis.

#### 4. Steady-state pressure-confined gas

In this work, we focus on how time-independent density patterns,

$$\frac{\partial \rho}{\partial t} = 0,\tag{9}$$

can be established under external pressure. A solution with no internal motion,

$$\mathbf{V} = 0, \tag{10}$$

represents a steady state, while a solution with time-independent internal velocity,

$$\frac{\partial \mathbf{V}}{\partial t} = 0,\tag{11}$$

represents an equilibrium state. Clearly, a steady state is a more restrictive condition than equilibrium.

Let  $\Omega$  denote the region occupied by the gas, with boundary  $S = \partial \Omega$ . We consider an isothermal gas confined within  $\Omega$  by a

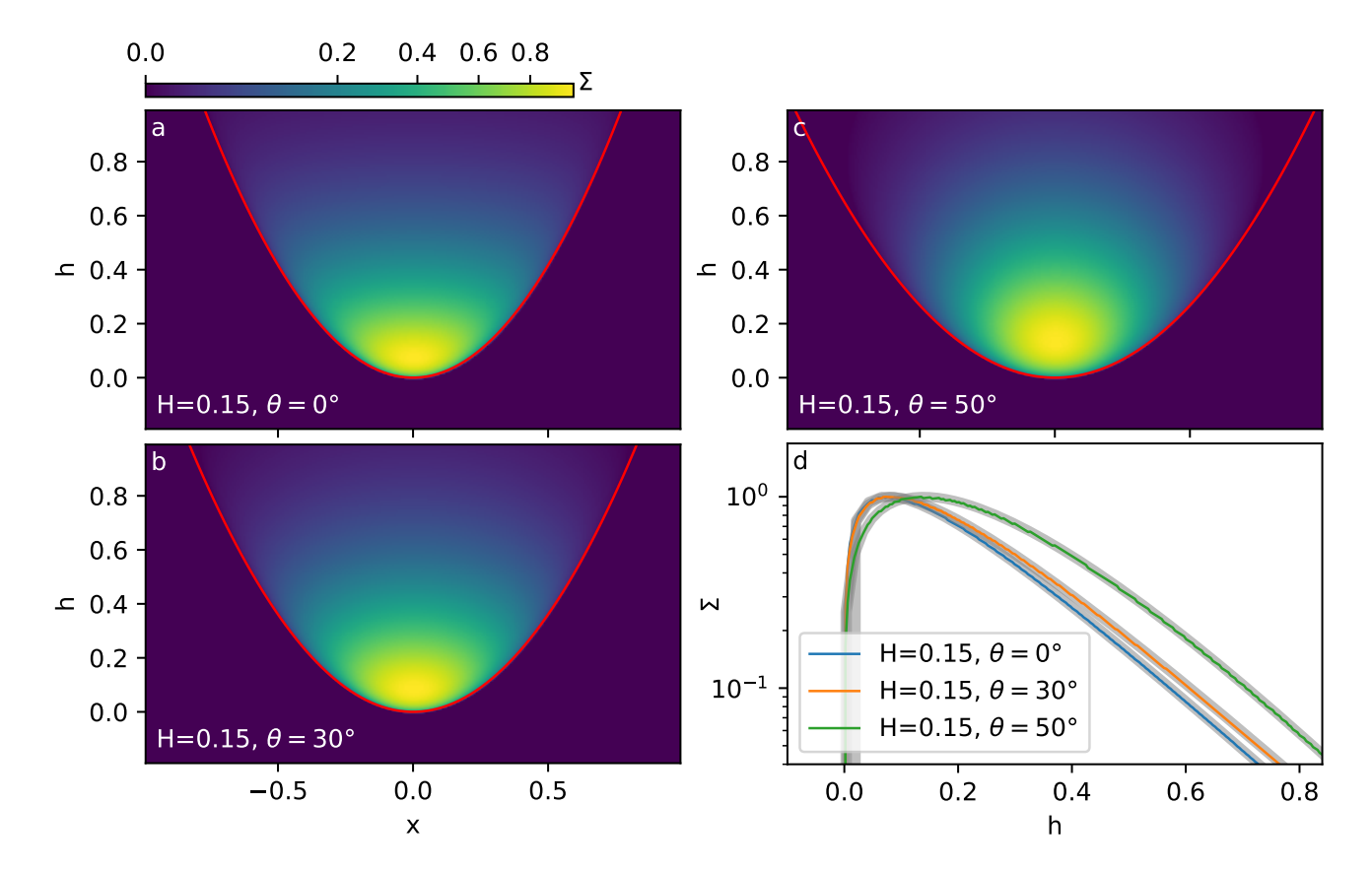


**Fig. 7.** Panels a—c: Surface densities (Eq. 41) from the 3D numerical construction based on the steady-state solution described in Sect. 4.2, shown for different zenith angles (white labels). The surface density maps are normalized to a maximum value of one. The red line in each panel marks the analytic boundary given by Eq. 45. Panel d: Surface densities along the projected axis (colored lines) compared with the analytic solution from Sect. 4.3 (thick gray line).

prescribed boundary pressure  $p_S$  on S, with no fluid crossing the boundary,

$$(\mathbf{V} \cdot \mathbf{n})|_{\mathbf{c}} = 0, \tag{12}$$

where  $\mathbf{n}$  is the outward normal to S. The gas obeys the ideal isothermal equation of state,

$$p = T\rho, \tag{13}$$

with scaled temperature

$$T = \frac{k_B}{\mu m_H} T_{\text{phys}},\tag{14}$$

where  $\mu$  is the mean molecular weight,  $m_{\rm H}$  the hydrogen mass,  $k_B$  the Boltzmann constant, and  $T_{\rm phys}$  the physical temperature. For this equation of state, along any fluid loop with a time-independent velocity, the Bernoulli equation (see, e.g., textbooks on fluid dynamics, Kundu & Cohen 2008) holds:

$$\frac{1}{2}\mathbf{V}^2 + T\ln(\rho) + \Phi = B_c,\tag{15}$$

where  $B_c$  is constant along a given loop but may differ between loops.

#### 4.1. Steady state under global acceleration

As the simplest special case of equilibrium, a steady state is achieved, in which the system is irrotational and viscosity plays

no role. Consequently, the Bernoulli equation (see Eq. 15) applies throughout the system. For V=0, it reduces to

$$T\ln(\rho) + \Phi = 0, (16)$$

where  $\Phi$  is a conservative scalar potential, allowing the Bernoulli constant to be absorbed into  $\Phi$ . This equation represents a balance between the potential  $\Phi$  and the boundary pressure  $p_S$  (or equivalently the density  $\rho$ ), which in turn determines the boundary potential  $\Phi_S$ .

If  $\Phi$  is a conservative potential, e.g., the gravitational potential due to external sources,

$$\nabla^2 \Phi \big|_{\Omega} = 0, \tag{17}$$

then  $\Phi$  inside the region  $\Omega$  is uniquely determined by its boundary values. The corresponding density (and pressure) follows as

$$\rho = \exp\left(-\frac{\Phi}{T}\right),\tag{18}$$

reproducing the standard result from equilibrium statistical mechanics.

In this work, we approximate  $\Phi$  as a linear scalar potential corresponding to a uniform acceleration, representing either a uniform gravitational field  ${\bf g}$  or an imposed global acceleration  ${\bf a}$ . This approximation is valid for a region small compared to the scale over which the gravitational field varies, so that tidal forces can be neglected. The potential can then be expressed as

$$\Phi(\mathbf{r}) = -\mathbf{a}_{\text{eff}} \cdot \mathbf{r}, \quad \mathbf{a}_{\text{eff}} = \mathbf{a} - \mathbf{g}. \tag{19}$$

In steady state, the gas exhibits an exponential density distribu-

$$\rho(\mathbf{r}) \propto \exp\left(-\frac{\Phi(\mathbf{r})}{T}\right),$$
(20)

with a characteristic scale height

$$H = \frac{T}{\|\mathbf{a}_{\text{eff}}\|}. (21)$$

The boundary pressure  $p_S$  is not arbitrary, but must follow the same exponential form as Eq. (20).

#### 4.2. Geometry under ram-pressure deceleration

Consider a gas exposed to an external flow with density  $\rho_{\rm ext}$  and velocity  $\mathbf{v}_{ram}$  across a cross-sectional area A. The force exerted by the ram pressure can be approximated as

$$F_{\text{ram}} \sim \rho_{\text{ext}} ||\mathbf{v}_{\text{ram}}||^2 A,$$
 (22)

and the mass per unit area of the gas is

$$\Sigma = \frac{M}{4}.\tag{23}$$

The resulting acceleration of the gas is then

$$a \sim \frac{F_{\text{ram}}}{M} = \frac{\rho_{\text{ext}} ||\mathbf{v}_{\text{ram}}||^2}{\Sigma}.$$
 (24)

This sets the characteristic scale height of the internal gas along the direction of the ram pressure,

$$H \sim \frac{T}{a} = \frac{T \Sigma}{\rho_{\text{ext}} ||\mathbf{v}_{\text{ram}}||^2}.$$
 (25)

In sect. 6.1, we will discuss the density of the external medium

Assuming the external flow comes from the negative zdirection,

$$\mathbf{v}_{\text{ram}} = \|\mathbf{v}_{\text{ram}}\|\,\hat{\mathbf{z}},\tag{26}$$

the flow is deflected at the interaction surface, becoming tangent to it. Thus, the shape of the surface is governed by the balance between the ram pressure of the external flow and the internal gas pressure.

In the axisymmetric case, we define the cylindrical radius

$$r = \sqrt{x^2 + y^2}. (27)$$

For a surface described by z(r), the outward normal **n** forms an angle  $\alpha$  with the z-axis, reducing the effective ram pressure perpendicular to the surface by a factor

$$\cos^2 \alpha = \frac{1}{1 + \left(\frac{dz}{dr}\right)^2}. (28)$$

The pressure balance at the surface can then be written as

$$\frac{1}{1 + \left(\frac{dz}{dt}\right)^2} p_0 = p_0 \exp\left(-\frac{z}{H}\right),\tag{29}$$

where

$$p_0 = \rho_{\text{ext}} \|\mathbf{v}_{\text{ram}}\|^2 \tag{30} \quad \Delta L = \frac{\Delta y}{\cos \theta}.$$

Article number, page 8 of 17

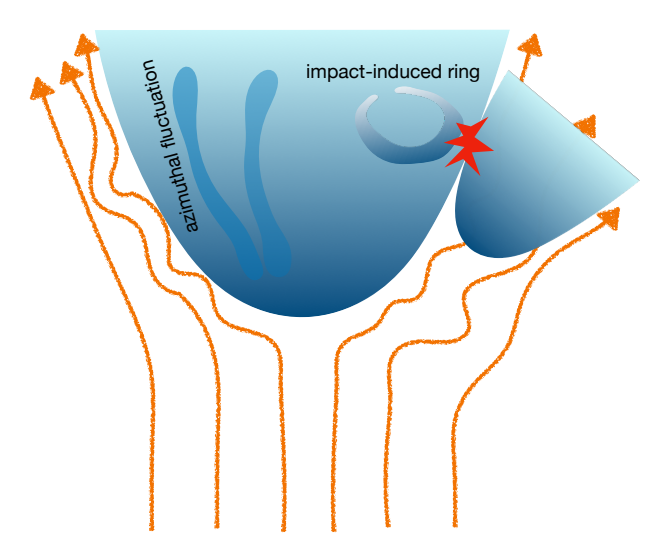


Fig. 8. Dynamic patterns in ram-pressure confined droplets. The rotating ring redistributes momentum and balances interactions between neighbouring droplets. Density strips along the boundary and axis are induced by turbulence in the high-Reynolds-number surrounding flows (Sect. 5.3).

is the characteristic ram pressure of the external flow. Solving Eq. 29, the surface profile is

$$z(r) = -2H \ln \left[ \cos \left( \frac{r}{2H} \right) \right], \qquad r < \frac{\pi H}{2}. \tag{31}$$

For small r, this reduces to the familiar parabolic form

$$z(r) \sim \frac{r^2}{4H}.\tag{32}$$

#### 4.3. Projection of steady-state geometry

Consider the intersection between the parabola

$$z = \frac{y^2}{4H} \tag{33}$$

and a straight line (tilted front)

$$z = \tan \theta \, y + z',\tag{34}$$

where z' is the line offset. Solving

$$\frac{y^2}{4H} = \tan\theta \, y + z' \tag{35}$$

yields the two intersection ordinates

$$y_{1,2} = 2H \tan \theta \mp 2\sqrt{H^2 \tan^2 \theta + Hz'},$$
 (36)

with corresponding heights

$$z_{1,2} = \tan\theta \, y_{1,2} + z'. \tag{37}$$

The horizontal separation is

$$\Delta y = y_2 - y_1 = 4\sqrt{H^2 \tan^2 \theta + Hz'},\tag{38}$$

and the line-segment length along the tilted front is

$$\Delta L = \frac{\Delta y}{\cos \theta}.\tag{39}$$

The local density at the near intersection is

$$\rho_1 = \rho_0 \exp\left(-\frac{z_1}{H}\right). \tag{40}$$

Along the segment, the vertical coordinate increases as z(s) = $z_1 + s \sin \theta$  with s the distance along the segment, so the density decays as  $\exp(-s\sin\theta/H)$ . Therefore, the exact line integral of the density over the segment is

$$I = \rho_1 \Delta L \frac{1 - \exp(-\Delta L \sin \theta / H)}{\Delta L \sin \theta / H}.$$
 (41)

This reduces to  $I \simeq \rho_{\text{head}} \Delta L$  when  $\Delta L \sin \theta \ll H$ , and to  $I \simeq$  $\rho_{\rm head} (H/\sin \theta)$  when  $\Delta L \sin \theta \gg H$ . Real intersections exist only

$$H^2 \tan^2 \theta + Hz' \ge 0, (42)$$

that is.

$$z' > -H \tan^2 \theta. \tag{43}$$

The projected distance of the head along the axis is

$$h = (z' + H \tan^2 \theta) \cos \theta. \tag{44}$$

The projected scale height  $(H_{\text{vert}})$  of the exponential tail of the intensity profile along the middle axis shows little change with h, and is slightly smaller for  $\theta > 0$  than for  $\theta = 0$  (Figure 7).

The projected radius of the boundary is reached at y = $2H \tan \theta$ , giving

$$R = \sqrt{4H^2 \tan^2 \theta + 4Hz'} = 2\sqrt{\frac{Hh}{\cos \theta}}.$$
 (45)

Thus, the projected boundary also follows a parabolic curve, with a magnification factor of  $1/\cos\theta$  compared to the untilted case (Eq. 32). The scale height obtained from fitting the horizontal width is

$$H_{\text{hori}} = H/\cos\theta. \tag{46}$$

#### 5. Equilibrium via internal turbulence

For an equilibrium state, as opposed to an instantaneous steady state, the situation is generally more complex. When the external pressure profile deviates from a simple exponential form, maintaining equilibrium would require a correspondingly complex external potential  $\Phi$ , which is rarely satisfied in practice. Instead, the system typically responds by developing an anisotropic stress tensor (e.g., a Rynoid tensor) to support the resulting pressure gradients. In principle, the fully general equilibrium problem is therefore very complicated

#### 5.1. Vorticity-induced Bernoulli balance

This subsection summarizes standard results from classical fluid dynamics for completeness. We consider an equilibrium, compressible, isothermal ideal gas, for which momentum conservation in steady state reads

$$\nabla \cdot (\rho \mathbf{V} \mathbf{V}) + \nabla p = -\rho \nabla \Phi, \tag{47}$$

where V is the velocity,  $\rho$  the density,  $p = T\rho$  the isothermal pressure, and  $\Phi$  an external potential.

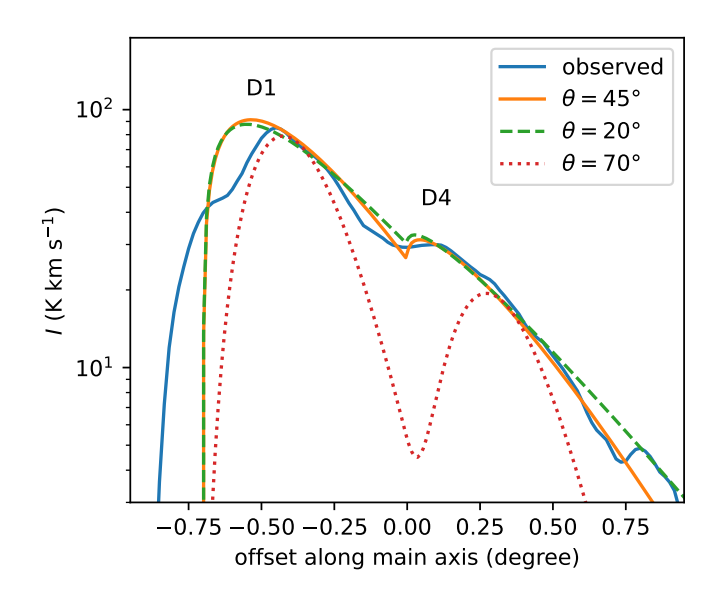


Fig. 9. HI integrated intensity (proportional to column density) along the main axis of D1 (blue solid line). The orange, green, and red curves show two-component fits assuming different inclination angles, as described in Sect. 4.2.

For  $\partial \rho / \partial t = \nabla \cdot (\rho \mathbf{V}) = 0$  (Eq. 9), this becomes

$$(\mathbf{V} \cdot \nabla)\mathbf{V} = -T\nabla \ln \rho - \nabla \Phi, \tag{48}$$

which can be rewritten as

$$\nabla \underbrace{\left(\frac{1}{2}|\mathbf{V}|^2 + T\ln\rho + \Phi\right)}_{R} = \mathbf{V} \times (\nabla \times \mathbf{V}),\tag{49}$$

where  $B_c$  is the Bernoulli quantity (Eq. 15).

Along a streamline, the Bernoulli quantity is conserved:

$$\mathbf{V} \cdot \nabla B_c = 0. \tag{50}$$

Perpendicular to streamlines, the balance is set by vorticity:

$$\nabla_{\perp} B_c = (\nabla \times \mathbf{V}) \times \mathbf{V},\tag{51}$$

accounting for centrifugal effects.

For rigid-body rotation in a plane,  $V = \Omega \times r$  with constant  $\Omega$ , the vorticity is uniform,  $\nabla \times \mathbf{V} = 2\Omega$ , and

$$(\nabla \times \mathbf{V}) \times \mathbf{V} = -\nabla |\mathbf{V}|^2. \tag{52}$$

Substituting this into Eq. 49 gives

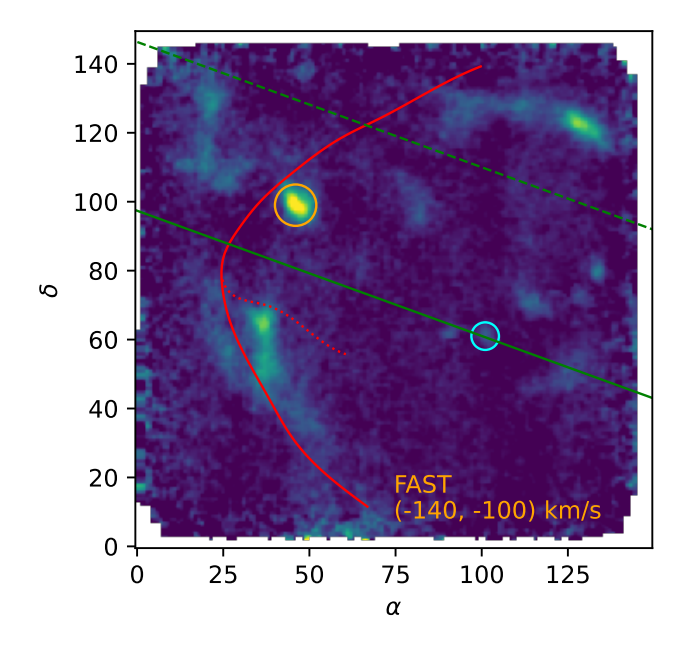
$$T\ln\rho + \Phi - \frac{1}{2}|\mathbf{V}|^2 = \text{const},\tag{53}$$

where  $-\frac{1}{2}|\mathbf{V}|^2$  acts as the centrifugal potential.

#### 5.2. Turbulence perspective

In the general case where deformation and rotation coexist, the Bernoulli balance (Eqs. 15 and 53) across streamlines for a single eddy can be written in the effective form

$$\frac{\alpha \frac{1}{2} |\mathbf{V}|^2 + T \ln \rho + \Phi = \text{const},}{\frac{1}{1} \text{ Note that } (\mathbf{V} \cdot \nabla) \mathbf{V} = \nabla \frac{|\mathbf{V}|^2}{2} - \mathbf{V} \times (\nabla \times \mathbf{V}).}$$
 (54)



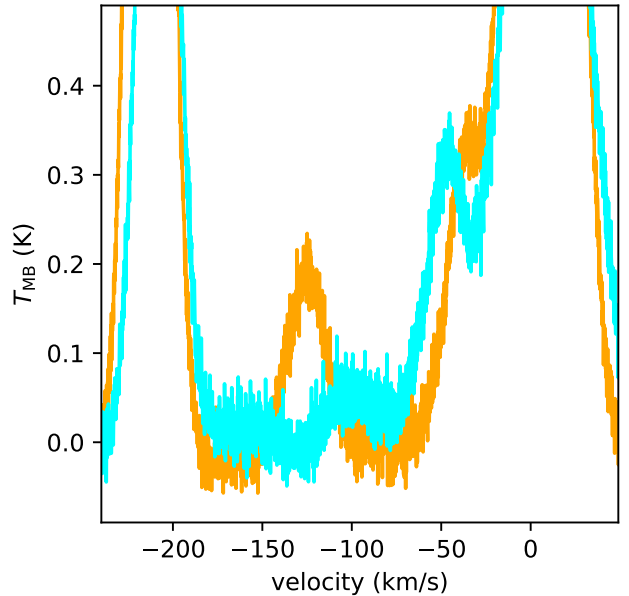


**Fig. 10.** Upper: Moment 0 map of the H  $_{\rm I}$  emission for the IVC component, integrated over -140 to -100 km s $^{-1}$ . The red solid and dashed lines mark D1, corresponding to the blue lines in the upper panel of Figure 2. Green lines indicate two position–velocity cuts, identical to the black lines in Figure 1. Lower: Example spectra of the IVC component for two clumps, shown in orange and cyan, located at the positions marked by circles of the same colors in the upper panel.

where  $\alpha$  represents the net effect of local deformation and rotation. Deformation-dominated flows correspond to  $\alpha \to 1$ , while rotation-dominated flows correspond to  $\alpha \to -1$ . In complex flow fields,  $\alpha$  can be interpreted as an integral quantity capturing the combined effect of multiple interacting eddies.

We now interpret turbulence support using this Bernoulli framework. On large scales, near the turbulence driving scale, the flow is quasi-steady and often dominated by coherent rotational or shearing structures. In this regime, the Bernoulli-like balance reads

$$-\frac{1}{2}|\mathbf{V}_{ls}|^2 + T\ln(\rho) + \Phi = \text{const},$$
 (55)

Article number, page 10 of 17

where the negative kinetic term provides centrifugal support against local pressure enhancements, sustaining turbulent motions.

At smaller scales, the flow becomes increasingly isotropic and intermittent. Following Kolmogorov (K41) scaling (Frisch 1995), the eddy turnover time  $l/v_l$  decreases with scale l, so small-scale motions cannot maintain long-lived coherent rotation. When averaged over a large-scale density  $\bar{\rho}$ , these small-scale fluctuations largely cancel, leaving a net isotropic contribution that acts as an effective thermal support,

$$T_{\text{eff}} = T + |\mathbf{V}_{\text{ss}}|^2,\tag{56}$$

which requires

$$\alpha_{\text{net}} |\mathbf{V}_{\text{ss}}|^2 \sim |\mathbf{V}_{\text{ss}}|^2 \ln(\bar{\rho}),$$
 (57)

so that the Bernoulli-like balance reads

$$T_{\text{eff}} \ln(\bar{\rho}) + \Phi \simeq \text{const.}$$
 (58)

At local scales, velocity fluctuations appear as random, isotropic increments. Over each unit interval in logarithmic  $\ln(T+V_{\rm ss}^2)$ , the Bernoulli coefficient  $\alpha$  is refreshed and produces a stochastic contribution of order unity, analogous to Eq. 57. Here, T represents the baseline kinetic contribution, while  $V_{\rm ss}^2$  encodes typical local compressions. The resulting microscopic-to-mesoscopic stochastic effect can be expressed as

$$T\ln(\rho) + \mathcal{N}\sqrt{\ln\left(1 + \frac{V_{ss}^2}{V_T^2}\right)}V_T^2 = \text{const}, \quad V_T^2 = T,$$
 (59)

where N is a standard Gaussian random variable. Slow, large-scale variations  $\Theta$  are omitted for clarity. This naturally leads to a lognormal density distribution with variance

$$\sigma_s^2 = \ln(1 + \mathcal{M}^2),\tag{60}$$

where  $\mathcal{M}$  is the Mach number, consistent with the thermodynamic view of turbulence (Liu 2025).

#### 5.3. Dynamic patterns under anisotropic pressure

A gas clump subjected to overpressure along a single direction, e.g., gravity or an equivalent acceleration field, can maintain steady state through an exponential density profile. When the external forcing is complex and multi-directional, no static density configuration can fully compensate the imposed stresses. Internal momentum flows arise to redistribute mass and energy, naturally organizing into coherent ring-like or toroidal loops (Figure 8). Rotation within these loops produces centrifugal forces that locally counteract the overpressure, providing effective dynamic support under anisotropic confinement. The formation and interaction of such loops maintain long-lived internal motions, inject vorticity and kinetic energy into the surrounding gas, and drive secondary turbulence (Sect. 5.2).

These internal motions can be further influenced by the surrounding medium, where time-dependent external flows modulate the clump's surface. External flows characterized by a high Reynolds number (Sect. 6.2) exert strong and fluctuating pressures on the droplet surface. These pressure variations induce small-scale density perturbations on the axisymmetric, parabolic surface of the droplet, forming alternating ridges and depressions. When seen in projection, these surface modulations appear as strip-like density structures roughly aligned with the droplet's main axis (Figure 8).

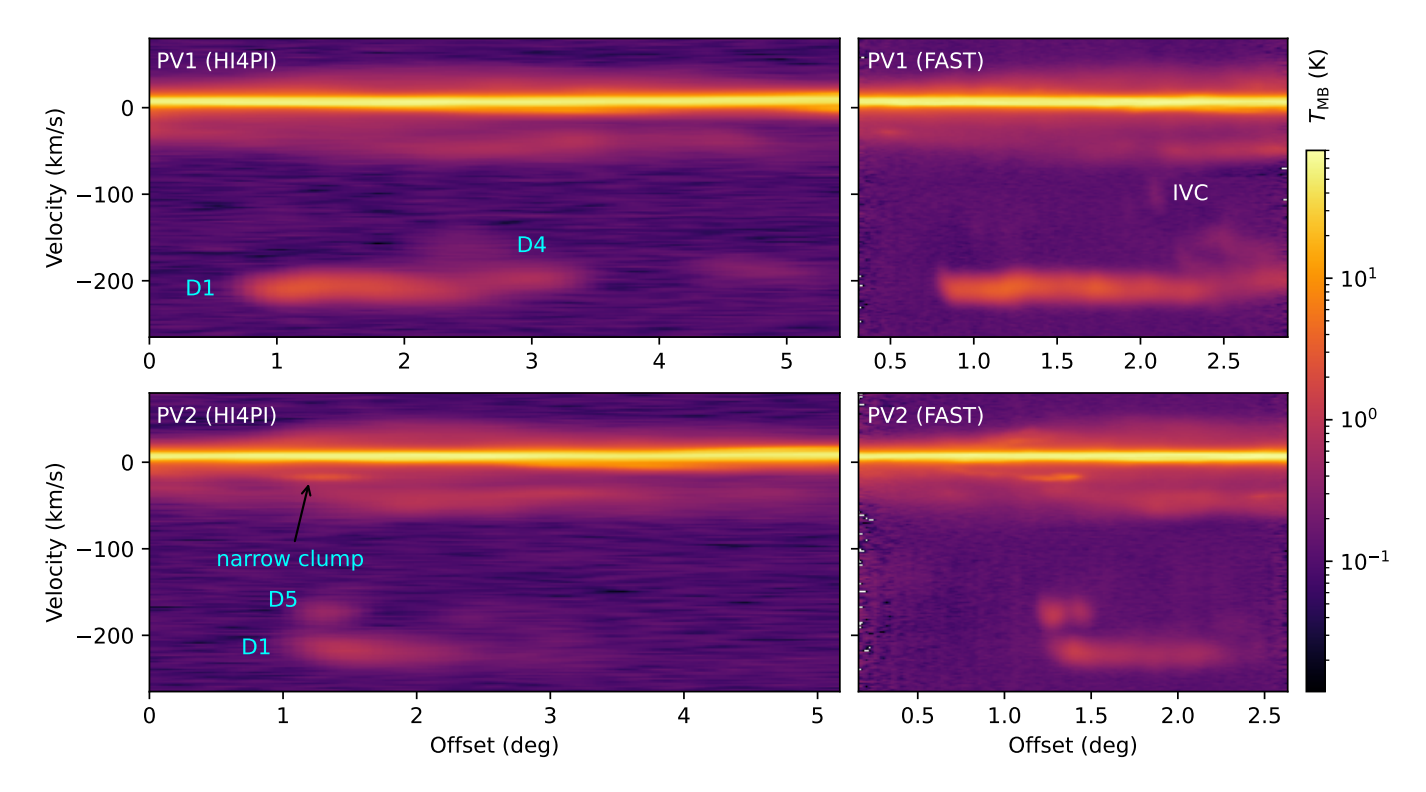


Fig. 11. Position-velocity (PV) maps along two cuts (PV1 in the top panels and PV2 in the bottom panels) are shown for H  $_14$ PI (left) and FAST (right) data. The emission from droplets (D1, D4, and D5), a narrow clump at low velocity ( $\sim 30 \text{ km s}^{-1}$ ), and an intermediate-velocity component (IVC) at  $\sim 100 \text{ km s}^{-1}$  are indicated (corresponding to the cyan circle in Figure 10).

Interactions between neighbouring droplets can further complicate both internal and external flows. In general, such interactions may simply result from intersecting trajectories. In the case of droplet D1 in AC-III, however, it is influenced by several neighbouring droplets located in different directions. This geometry suggests the existence of a specific mechanism that can effectively push neighbouring droplets together. One possibility is the Bernoulli effect: when the flow accelerates between adjacent droplets, a low-pressure region is created that draws the droplets closer (Eq. 15; Figure 8). These interactions can trigger internal loops, enhancing the complexity of gas motions and contributing to the overall dynamic behavior of the system

#### 6. Discussion

#### 6.1. AC-III dropping through the WIM

We can fit the scale height H and the number density at the tip of AC-III (Sect. 6.2), accounting for projection effects due to a non-zero inclination angle  $\theta$  following Sect. 4.3. However, the ram pressure can be robustly estimated using Eq. 25 without detailed modeling. The column density  $\Sigma$  along the main axis is of the same order of magnitude as that along other sight lines, and we adopt the value derived from a typical  $H_I$  integrated intensity of 50 K km s<sup>-1</sup> (Figure 2). The external flow velocity is estimated as

$$\|\mathbf{v}_{\text{ram}}\| \sim \sqrt{2} \times 200 \sim 300 \text{ km s}^{-1},$$
 (61)

accounting for projection effects. The scale height of the droplet is taken as  $d \times 0.25^\circ$ , and the internal temperature of AC-III is estimated from the line width as

$$T_{\text{eff}} \sim \left(\frac{\Delta V}{2}\right)^2, \quad \Delta V \sim 20 \text{ km s}^{-1}.$$
 (62)

The resulting number density of the external medium is

$$n_{\text{ext}} = \frac{\rho_{\text{ext}}}{m_H} \sim \frac{1.4 \times 10^{-3}}{d_5} \text{ cm}^{-3}.$$
 (63)

This estimate is consistent with the warm ionized medium (WIM; Reynolds 1991; Gaensler et al. 2008). Adopting a midplane WIM density of  $n_0 \sim 0.01 \text{ cm}^{-3}$  and a scale height  $H_{\text{WIM}} \sim 1 \text{ kpc}$  (Gaensler et al. 2008), the WIM density at the location of AC-III is

$$n_{\text{WIM}} \sim n_0 \exp\left(-\frac{d\sin b}{H_{\text{WIM}}}\right) \sim 8 \times 10^{-4} \exp(-d_5) \text{ cm}^{-3},$$
 (64)

consistent with Eq. 63. Therefore, AC-III is likely experiencing deceleration due to the WIM. Its infall velocity,  $\|\mathbf{v}_{ram}\|$ , is comparable to the local free-fall velocity under Galactic disk and halo gravity, suggesting that AC-III is located several kpc above the plane and is beginning to interact with the Galactic WIM layer.

If this scenario is correct, several implications follow. (1) Most HVCs may reside outside the Galactic WIM layer, since droplet-like morphologies are not common; this can be tested with higher-resolution observations. (2) HVCs may remain dominated by WNM until they begin to penetrate and are compressed by the WIM layer. Furthermore, systematic surveys of HVC morphologies could provide useful constraints on the scale height and density of the Galactic WIM layer.

#### 6.2. Droplet fitting

A parabolic fit to the head of D1 (blue solid curve in the upper panel of Figure 2) yields a horizontal scale  $H_{\rm hori} \sim 0.3^{\circ}$ . The column density profile along the main axis of D1 is shown in Figure 9. Due to neighboring droplets (e.g., D4 and D6) and

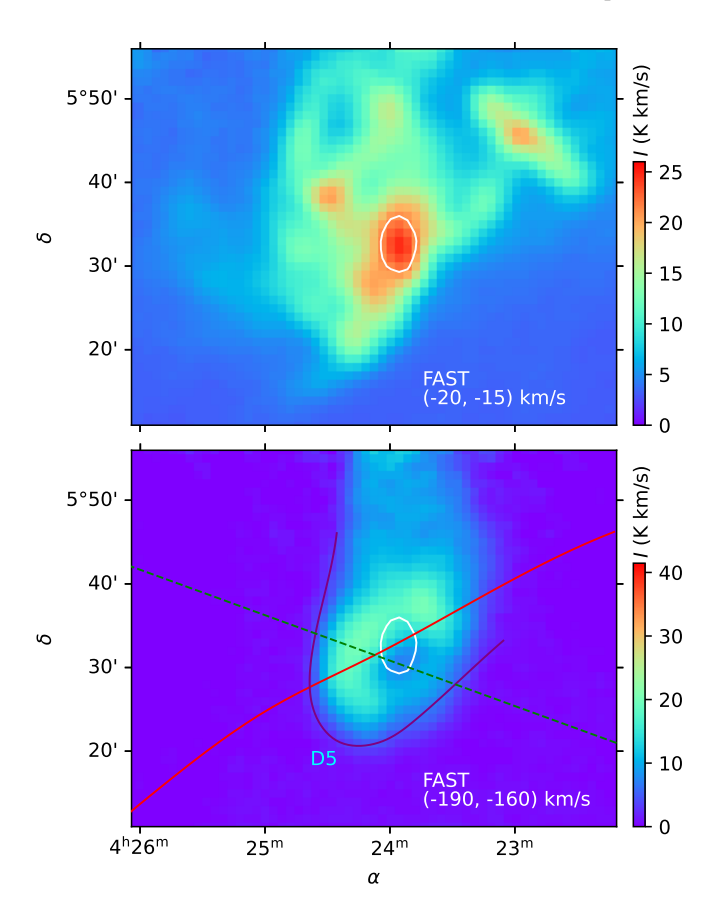


**Fig. 12.** Upper: Moment 0 map of the foreground narrow clump (see Figure 11), with the white contour at 20 K km s $^{-1}$ . Lower: Moment 0 map of D5, with the white contour identical to that in the upper panel. The red and purple lines indicate the heads of D1 and D5, respectively (see also the upper panel of Figure 4). The blue dashed line marks the position–velocity cut PV2 (see Figure 1).

their induced dynamical effects within D1, a single profile given by Eq. 41 cannot adequately reproduce the observed profile. Instead, we adopt two such profiles with the same H and inclination angle  $\theta$  to fit the observed profile.

Under the steady-state assumption, H is expected to decrease as  $\theta$  increases (Eq. 46), which would steepen the profile's tail. However, increasing  $\theta$  also softens the profile due to projection effects, making the resultant profile relatively insensitive to  $\theta$ . In Figure 2, we show that moderate values of  $\theta$ , e.g.,  $20^{\circ}$  or  $45^{\circ}$ , can reasonably reproduce the observed profile, whereas inclinations close to  $90^{\circ}$  are ruled out. This implies that AC-III cannot be moving purely along the line of sight; its velocity perpendicular to the line of sight is considerable.

Assuming an inclination angle of  $\theta = 45^{\circ}$ , the number density at the tip of the droplet is fitted to be  $n_{\rm tip} \sim 2 \, d_5^{-1} \, {\rm cm}^{-3}$ , about ten times the average value (Eq. 5). From Eq. 25, we have

$$n_{\text{ext}} \sim n_{\text{tip}} \frac{\|\mathbf{v}_{\text{internal}}\|^2}{\|\mathbf{v}_{\text{ram}}\|^2} \sim n_{\text{tip}} \frac{\|\mathbf{v}_{\text{internal}}\|^2}{\|\mathbf{v}_{\text{LOS}}/\cos\theta\|^2},$$
 (65)

where  $\mathbf{v}_{\text{internal}}$  is the velocity dispersion (including both thermal and turbulent motions; Eq. 56) at the tip, adopted as  $10 \text{ km s}^{-1}$  as in Sect. 6.1, and  $\mathbf{v}_{\text{LOS}}$  is the observed line-of-sight velocity. For  $\theta = 45^{\circ}$ , this yields  $n_{\text{ext}} \sim 2 \times 10^{-3} \text{ cm}^{-3}$ . Taking a smaller inclination, e.g.,  $\theta = 20^{\circ}$ , reduces  $n_{\text{tip}}$  to  $\sim 1.2 \, d_{5}^{-1} \, \text{cm}^{-3}$ , but results in a nearly unchanged  $n_{\text{ext}} \sim 2 \times 10^{-3} \, \text{cm}^{-3}$ . This demonstrates that the quantitative estimate in Sect. 6.1 is robust against pro-

jection effects, thereby reinforcing the validity of the associated interpretation (see further discussion in Sect. 6.4).

#### 6.3. Foreground and IVC components

The large line-of-sight velocity of AC-III, combined with its smooth, droplet-like morphology, implies that the cloud is moving through a medium with a density much lower than its own. Under these conditions, strong direct interactions between AC-III and lower-velocity H I associated with the Galactic disk are not expected. Secondary interactions, however, cannot be entirely excluded.

To investigate possible spatial or kinematic associations with lower-velocity H<sub>I</sub>, Figure 10 shows the moment 0 map of the IVC component, integrated over -140 to -100 km s<sup>-1</sup>. The IVC emission forms a shell-like structure roughly aligned with the head of D1. This shell is fragmented into compact clumps with sizes comparable to the FAST beam, some of which lie along the main axis of D1 (green solid line in Figure 10, PV1). These clumps are unresolved in the HI4PI survey due to its lower angular resolution and sensitivity. Example spectra of the IVC clumps, together with the PV diagram along PV1, indicate that the clumps occupy a velocity range closer to the foreground H<sub>I</sub> component. While the spatial alignment between the IVC and AC-III is observed, no direct kinematic connection is detected. Any secondary indirect interaction, for instance via pressuremediated effects in the WIM, cannot be assessed without additional data, such as accurate distance measurements and observations of the intervening ionized medium.

A similar spatial configuration is found near D5, where a compact clump at  $\sim -20 \text{ km s}^{-1}$  (hereafter the "narrow clump") exhibits a morphology comparable to D5, including a convex margin facing toward the Equinox west direction. The emission peak of the narrow clump coincides with H4, the emission hole within D5 (Figure 4). The line width of  $\sim 3 \text{ km s}^{-1}$  suggests that the clump primarily consists of cold neutral medium (CNM). No corresponding structures are identified in either the major or minor foreground H<sub>I</sub> components, which span velocity ranges of -10 to 20 km s<sup>-1</sup> and -50 to -20 km s<sup>-1</sup>, respectively. The position-velocity (PV) diagram reveals a clear emission gap between D5 and the narrow clump, indicating that any direct dynamical influence of AC-III on the narrow clump is limited. The observed morphological similarity is therefore most likely the result of projection effects or large-scale spatial alignment, rather than a physical interaction.

In summary, these observations provide a detailed account of the spatial and kinematic distributions of lower-velocity H I around AC-III. No direct interactions are detected, and any secondary connections remain undetermined. Further observational data, including precise distance measurements and characterization of the ionized medium, are required to evaluate possible links.

### 6.4. Reynolds number of external flows

The ambient gas, whether in the warm ionized medium (WIM) or the hot halo (Figure 13), consists of a fully ionized hydrogen plasma. Its kinematic properties are governed by Coulomb collisions, which determine the dynamic viscosity. The dynamic viscosity ( $\mu_d$ ) of a fully ionized hydrogen plasma can be expressed as (Spitzer & Härm 1953):

$$\eta = 2.21 \times 10^{-15} \frac{T^{5/2}}{Z^4 \ln \Lambda} \quad [\text{g cm}^{-1} \text{s}^{-1}],$$
(66)

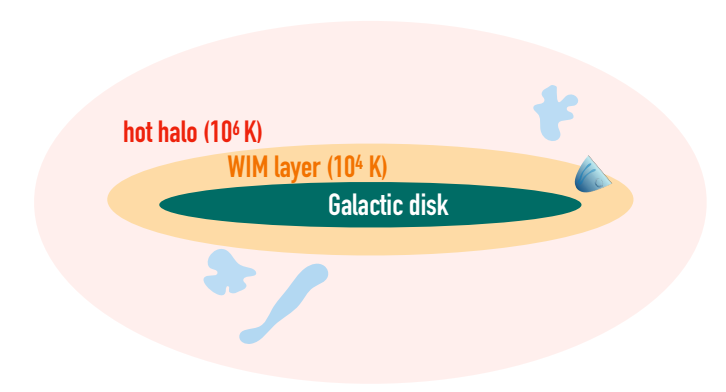


**Fig. 13.** Schematic of high-velocity clouds (HVCs) in the Galactic environment. AC-III (red) is shown interacting with the Warm Ionized Medium (WIM) layer wrapping the Galactic disk (Sect. 6.4), while most other HVCs (blue) reside at larger distances (several to tens of kpc) in the hot halo (Sects. 6.1 and 6.2).

where T is the temperature in Kelvin,  $\ln \Lambda$  is the Coulomb logarithm (typically  $\sim 30$ ), and Z is the charge number of the particle (e.g., Z = 1 for hydrogen).

The Reynolds number of the external flow is then

$$Re = \frac{VL\rho}{\eta} = \frac{VLn_{\text{ext}}m_p}{\eta},\tag{67}$$

with  $L \sim H$  for a droplet and  $m_p$  the proton mass (since protons dominate the momentum transport compared to electrons). Equation 67 can be simplified as

Re ~ 10 [
$$H d_5$$
]  $\left[ \frac{T}{10^6 \text{ K}} \right]^{-5/2} \left[ \frac{V_{\text{ext}}}{200 \text{ km s}^{-1}} \right] \left[ \frac{n_{\text{ext}}}{10^{-4} \text{ cm}^{-3}} \right],$  (68)

where H is the angular size in degrees. The Reynolds number decreases dramatically as the temperature increases.

For a typical droplet (with an angular size of  $H \sim 1^{\circ}$  and moving at  $V_{\rm ext} = 200~{\rm km~s^{-1}}$ ), adopting parameters typical of the WIM ( $n_{\rm ext} = 10^{-3}~{\rm cm^{-3}}$ ,  $T \sim 10^4~{\rm K}$ ) yields a very large Reynolds number of Re  $\sim 10^7$ . Adopting parameters typical of the hot halo ( $n_{\rm ext} = 10^{-4}~{\rm cm^{-3}}$ ,  $T \sim 10^6~{\rm K}$ ) results in Re  $\sim 10$ . Note that the thermal velocity dispersion at  $10^6~{\rm K}$  is  $\sim 100~{\rm km~s^{-1}}$ , comparable to the typical moving velocity of HVCs, while the thermal dispersion at  $10^4~{\rm K}$  is  $\sim 10~{\rm km~s^{-1}}$ , much smaller than the typical moving velocity of HVCs. Thus, a droplet tends to move relatively smoothly in the hot halo at transonic or subsonic speeds, where the external fluid has a moderate Reynolds number, while it experiences strongly turbulent flows when entering the colder and denser WIM regime at supersonic speeds. The net deceleration effect of ram pressure depends on the departure of fluid stream from the body surface. The effective A (Eq. 22) thus could reach the droplet surface for high Reynolds number case, explaining both the significant decelerating and surface fluctuation of droplet AC-III.

## 7. Summary

The FAST H<sub>I</sub> observations reveal unprecedented inner structures of the HVC AC-III. We analyzed the morphologies and dynamical patterns of AC-III, and our main findings include:

(1) HVC AC-III can be divided into several subclumps (denoted D1 through D6), each with a nearly constant line width of  $\sim 20 \text{ km s}^{-1}$  and a mean number density of  $\sim 0.2 \text{ cm}^{-3}$ .

- However, the global velocity distribution of AC-III is broad, spanning -220 to -180 km s<sup>-1</sup>. This implies that each subclump in AC-III is a coherent parcel of transonic or subsonic WNM, with most of the dynamical energy stored in clump-to-clump motions.
- (2) These subclumps exhibit a parabolic morphology, which can be interpreted as droplets confined by ram pressure. In steady state, the deceleration caused by ram pressure is equivalent to the introduction of a linear potential, compressing the gas toward the tip, consistent with the observations.
- (3) A steady-state fit yields a tip peak density of  $\sim 2 \text{ cm}^{-3}$ , about ten times higher than the average density. This corresponds to an external medium density of  $\sim 10^{-3} \text{ cm}^{-3}$ , comparable to the density of the Galactic WIM layer at the location of AC-III (assuming a distance of 5 kpc). Although the inclination angle ( $\theta$ ) cannot be precisely constrained, there must be a non-negligible angle between the line of sight and the moving direction of AC-III, indicating that the velocity perpendicular to the line of sight is considerable.
- (4) The droplets in AC-III may be shaped by ram pressure as they enter the Galactic WIM layer. Since droplet-like morphologies are uncommon, most HVCs likely reside outside the WIM layer. From a dynamical perspective, we suggest that HVCs generally lie at moderate distances—several to roughly ten kiloparsecs—placing them in the inner halo rather than in the outer halo or intergalactic space.
- (5) The main droplet, D1, deviates from the symmetric steadystate morphology. This may be induced by interactions with neighboring droplets. In addition, strip-, ring-, and holelike structures can be observed within the droplets, implying complex dynamical motions that are responsible for these patterns.
- (6) The IVC component (with velocities from -150 to -100 km s<sup>-1</sup>) presents a shell-like morphology aligned with the head of AC-III. The PV maps show no direct connection between the IVC and HVC components. However, indirect physical links, for example via large-scale perturbations in the WIM (e.g., density waves), cannot be excluded.
- (7) Within the framework of the Bernoulli equation, we present a schematic of ram-pressure—induced droplets. Under steady ram pressure, a droplet develops a parabolic morphology and an exponential density profile. Ram pressure also tends to drive neighboring droplets to merge. The turbulence of the external flow, due to the high Reynolds number, may induce density ridges on the droplet surface, giving rise to the observed strip-like structures. Internal fluid loops arise naturally in response to anisotropic pressures, such as droplet interactions, and form ring-like stable patterns that can persist over long timescales. These fluid loops may further stimulate secondary turbulence within the droplets.

Overall, HVC AC-III is entering the Galactic WIM layer and being sculpted by ram pressure into a droplet-like morphology. It provides a valuable case to study the dynamical evolution of HVCs and the physical properties of the ambient medium.

Acknowledgements. We thank the FAST staff for their assistance during the observations. X.L. acknowledges support from the Strategic Priority Research Program of the Chinese Academy of Sciences under Grant No. XDB0800303.

#### References

Barone, T. M., Kacprzak, G. G., Nightingale, J. W., et al. 2024, Communications Physics, 7, 286

Blagrave, K., Martin, P. G., Joncas, G., et al. 2017, ApJ, 834, 126

Bregman, J. N. 1980, ApJ, 236, 577

Cashman, F. H., Fox, A. J., Wakker, B. P., et al. 2023, ApJ, 944, 65

Condon, J. J., Cotton, W. D., Greisen, E. W., et al. 1998, AJ, 115, 1693

de Boer, K. S. 2004, A&A, 419, 527

Fox, A. J., Lehner, N., Lockman, F. J., et al. 2016, ApJ, 816, L11

Frisch, U. 1995, Turbulence. The legacy of A.N. Kolmogorov

Gaensler, B. M., Madsen, G. J., Chatterjee, S., & Mao, S. A. 2008, PASA, 25, 184

Haffner, L. M., Dettmar, R. J., Beckman, J. E., et al. 2009, Reviews of Modern Physics, 81, 969

Heiles, C. & Troland, T. H. 2003, ApJ, 586, 1067

HI4PI Collaboration, Ben Bekhti, N., Flöer, L., et al. 2016, A&A, 594, A116

Holm-Hansen, C., Putman, M. E., & Kim, D. A. 2025, MNRAS, 536, 3507

Holm-Hansen, C., Putman, M. E., Kim, D. A., & Clark, S. E. 2024, in American Astronomical Society Meeting Abstracts, Vol. 243, American Astronomical Society Meeting Abstracts, 402.24

Jiang, P., Yue, Y., Gan, H., et al. 2019, Science China Physics, Mechanics, and Astronomy, 62, 959502

Kalberla, P. M. W. & Kerp, J. 2009, ARA&A, 47, 27

Kundu, P. K. & Cohen, I. M. 2008, Fluid Mechanics: Fourth Edition

Li, D. & Goldsmith, P. F. 2003, ApJ, 585, 823

Liu, X. 2025, arXiv e-prints, arXiv:2502.20458

Liu, X., Liu, T., Li, P.-S., et al. 2025a, Nature Astronomy, 9, 1366

Liu, X., Liu, T., Li, P.-S., et al. 2025b, Nature Astronomy [arXiv:2502.10897]

Liu, X., Wu, Y., Zhang, C., et al. 2022, A&A, 658, A140

Lockman, F. J., Benjamin, R. A., Heroux, A. J., & Langston, G. I. 2008, ApJ, 679, L21

McClure-Griffiths, N. M., Stanimirović, S., & Rybarczyk, D. R. 2023, ARA&A, 61, 19

Nan, R., Li, D., Jin, C., et al. 2011, International Journal of Modern Physics D, 20, 989

Peek, J. E. G., Bordoloi, R., Sana, H., et al. 2016, ApJ, 828, L20

Reynolds, R. J. 1991, ApJ, 372, L17

Shapiro, P. R. & Field, G. B. 1976, ApJ, 205, 762

Spitzer, L. & Härm, R. 1953, Physical Review, 89, 977

Tamanaha, C. M. 1996, ApJS, 104, 81

Thom, C., Peek, J. E. G., Putman, M. E., et al. 2008, ApJ, 684, 364

van Woerden, H., Schwarz, U. J., Peletier, R. F., Wakker, B. P., & Kalberla, P. M. W. 1999, Nature, 400, 138

Wakker, B. P. 1991, A&A, 250, 499

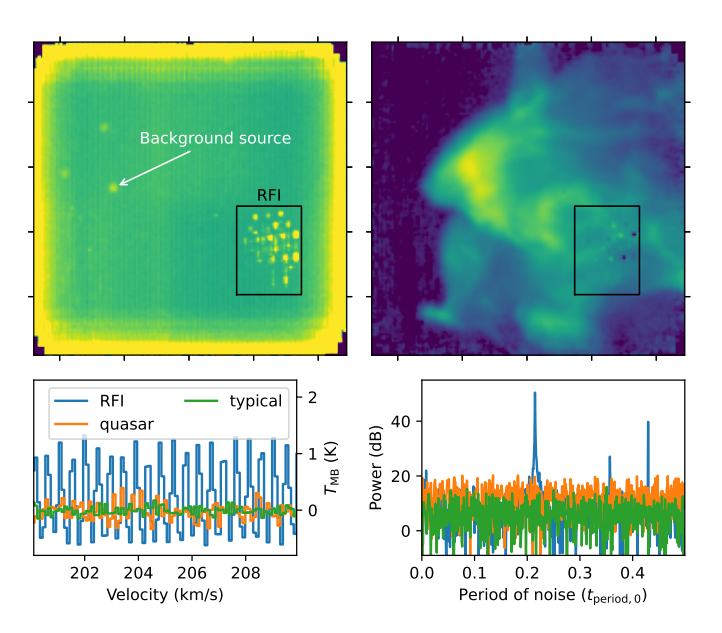
Wakker, B. P., York, D. G., Wilhelm, R., et al. 2008, ApJ, 672, 298

Westmeier, T. 2018, MNRAS, 474, 289

#### **Appendix A: Issues in Data Reduction**

Figure 1 shows the moment-0 map of AC-III as revealed by HI4PI (HI4PI Collaboration et al. 2016). The four OTF fields observed with FAST are also indicated. The FAST observations are described in Sect. 2, and the data reduction procedure follows Liu et al. 2025b.

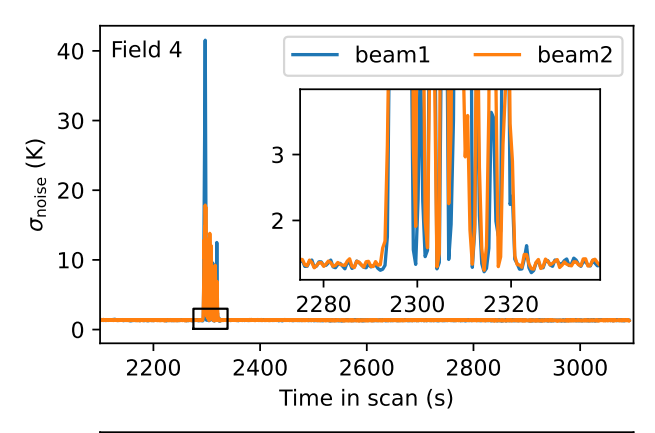
The noise map of the FAST data cube, obtained by calculating the standard deviation over the line-free channels, is relatively uniform in the central part of the mapped region, with higher values toward the margins due to limited scanning time and at the positions of bright background radio sources (usually quasars), as expected. In addition, some unexpected high-noise spots are present, which are enclosed by black squares in the upper left panel of Figure A.1. These features are likely caused by radio frequency interference (RFI), which severely affects the H I integrated intensity map at the corresponding pixels (see upper right panel of Figure A.1). Therefore, it is necessary to remove them before further analysis.



**Fig. A.1.** Upper left: One- $\sigma$  noise map of the RFI-contaminated FAST cube. The black box marks the RFI-affected region, and the white arrow points to the strongest background radio source. Upper right: H<sub>I</sub> map of AC-III integrated from the same cube. Lower left: Example spectra of RFI-affected pixels, pixels near the quasar, and normal pixels. Lower right: Fourier transform of the example spectra over  $100-200 \text{ km s}^{-1}$  (emission-line-free range), showing noise power versus period. Line colors correspond to the pixels shown in the lower-left panel.

#### Appendix A.1: Remove RFI

The RFI-affected pixels are distributed in a pattern corresponding to the 19 beams of the receiver, suggesting that the interference occurred within a short time interval and simultaneously affected all beams. In the lower left panel of Figure A.1, we compare representative spectra in a line-free velocity window from a pixel affected by RFI, a pixel near a quasar, and a normal pixel. The noise in the RFI-uncontaminated pixels (those near a quasar and normal pixels) appears visually white-noise-like, with the noise near the quasar showing a higher standard deviation. In contrast, the noise at the RFI-contaminated pixel is overwhelmed by a periodic comb function in the frequency domain, with a period of about four to five  $\delta f$ . The Fourier trans-



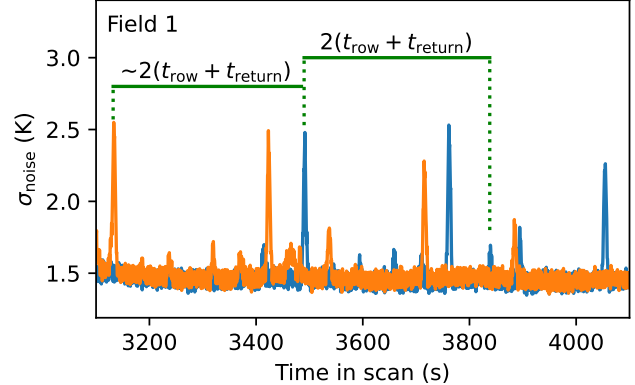


**Fig. A.2.** Upper: Noise level versus time for Field 4, with intervals affected by strong RFI highlighted. The inset shows a zoomed-in view of the region indicated by the black box. Different colors represent different beams. Lower: Noise level for a time segment from Field 1, showing the effect of background radio sources. Green lines mark noise enhancements separated by time intervals of  $2(t_{\text{row}} + t_{\text{treturn}})$ , corresponding to the same sources being observed twice by the same beam and by different beams along the same scan direction. For successive rows scanned in the opposite direction, the interval between noise peaks varies with the source position along the scan.

form of the noise spectra (within an emission-line-free velocity range of  $100-200 \, \mathrm{km \, s^{-1}}$ ), shown in the lower right panel of Figure A.1, confirms that the RFI-uncontaminated noise is indeed white noise in the period domain, whereas the RFI-contaminated noise has its power concentrated around three periods, with the most significant peak at  $t_{\mathrm{period}, \, \mathrm{RFI}} \sim 0.215 \, t_{\mathrm{period},0} \sim 0.45 \, \mathrm{ms}$ . Overall, the noise at certain pixels is strong, intermittent, and exhibits a comb-like pattern in the frequency domain, corresponding to a characteristic period of  $\sim 0.45 \, \mathrm{ms}$  in the time domain, in contrast to the visually white-noise–like behavior of normal pixels.

We plot the noise level of each sampled spectrum (with a sampling interval of  $\sim 0.5$  ms; see Sect. 2) as a function of sampling time and visually inspect the samples exhibiting abnormal noise. Only a single short time interval is found to contain obviously abnormal values, as shown in Figure A.2. This interval (RFI time interval) lasts about half a minute during the OTF scan of the fourth field. The noise contributed by the system temperature is  $\sim 1.5$  K, while the noise level can reach up to 40 K during the RFI interval. Note that the noise level also increases when the beams scan around background radio sources. The strongest radio source contributes to a noise level increase of  $\sim 1$  K. The noise increment caused by background radio sources can be easily recognized based on several characteristics: (1) the increase is

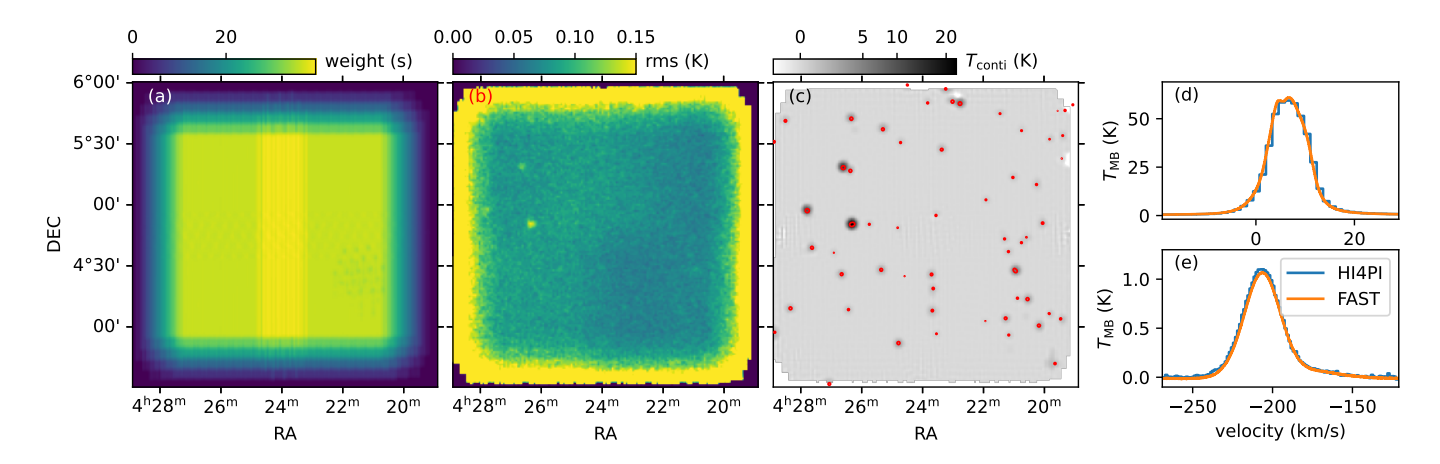


**Fig. A.3.** (a) Weight map of the OTF data after gridding, showing spatial coverage and relative sensitivity across the field. (b) One- $\sigma$  noise map of the cube after RFI removal, illustrating noise variations across different regions. (c) FAST *L*-band continuum map overlaid with NVSS L-band contours at 15 mJy beam<sup>-1</sup>, highlighting strong radio sources. (d)–(e) Comparison of mean spectra averaged over the observed region from FAST and HI4PI, for the foreground and high-velocity cloud (HVC) components, respectively.

not as strong as that induced by RFI; (2) the affected time interval is narrow, corresponding to the beam size divided by the scanning speed; (3) when the row separation is small, a radio source is covered by several successive rows of each beam, with every two visits separated by  $2(t_{\text{row}} + t_{\text{return}})$ ; (4) similar increments occur for all beams, but with a time delay, e.g., the increment in beam 2 is delayed by about  $2(t_{\text{row}} + t_{\text{return}})$  compared to beam 1 (see lower panel of Figure A.2). Here,  $t_{\text{row}}$  is the scanning time of each row (120 s).

In this work, to obtain the RFI-free merged cube, we simply discard the data within the RFI-contaminated time interval. Note that, since the 19 beams visit the same location at different times, a location affected by RFI in one beam can still be covered by the other 18 beams during non-RFI intervals. Therefore, the impact on the effective integration time and sensitivity is minimal.

#### Appendix A.2: Verification of RFI-cleaned data cube

The weight distribution from the OTF gridding is uniform across the mapped field (Figure A.3a), indicating that the removal of RFI-contaminated data does not affect the coverage. The rms noise of the final cube within the central  $1.5^{\circ} \times 1.5^{\circ}$  region is  $75 \pm 8$  mK at the native velocity resolution of  $\sim 0.1$  km s<sup>-1</sup> (Figure A.3b), and the RFI-induced spots on the noise map are removed as expected. The continuum map extracted from the dataset shows good agreement with the NVSS L-band continuum in both morphology and integrated flux density (Figure A.3c), with discrepancies within 5%. A two-dimensional Gaussian fit to the brightest background continuum source (upper left panel of Figure A.1) yields a FWHM beam size of 3.2' and a peak brightness temperature of 16.36 K, corresponding to a flux density of 1.03 Jy beam<sup>-1</sup>, consistent with the NVSS measurement of 1.08 Jy within 5% (Condon et al. 1998). The mean H<sub>I</sub> spectrum averaged over the observed field is likewise in good agreement with the HI4PI survey (HI4PI Collaboration et al. 2016) in both spectral profile and absolute intensity (panels d-e of Figure A.3).

#### Appendix A.3: Fourier-based comb interference removal

In this work, we excluded the data segments affected by strong RFI, as these events occurred over short time intervals and the

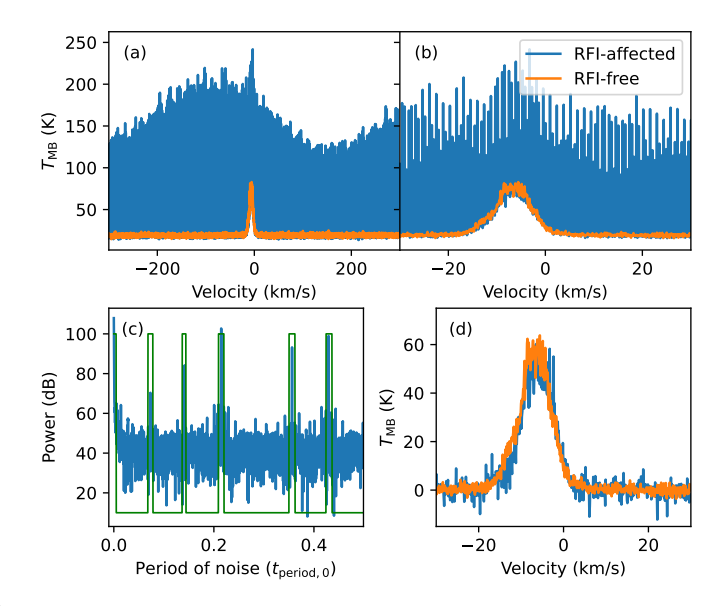


**Fig. A.4.** Panel (a): Spectrum with the strongest RFI contamination. The orange line shows the spectrum from a neighboring time sample that is not affected by RFI. Both spectra correspond to backend integrations with a sampling interval of  $\sim 0.5$  s (Sect. 2). Panel (b): Same as panel (a), but zoomed in to a narrower velocity range. Panel (c): Fourier transform of the example spectrum. The green line shows the mask ( $\mathcal{M}_k$ ; see Sect. A.3) applied to periods with abnormally high power. Panel (d): RFI-removed spectrum, compared with its neighboring spectrum.

OTF observations have redundant coverage due to the narrow row separation employed (Sect. 2). We also present a method to remove comb-like patterns in RFI-contaminated spectra using Fourier transform techniques, which may be useful in future analyses or for observations with less redundant coverage or more severe RFI contamination.

The spectrum with the strongest RFI contamination is shown as an example (see panels a and b of Figure A.4). The RFI is so severe that it dominates the signal, even compared to the foreground H  $\scriptstyle\rm I$  spectrum, which has a peak intensity of  $\sim 60$  K, as indicated by the spectrum from a neighboring time sample.

To identify periodic features induced by RFI, we apply a Fourier transform to the spectrum. The Fourier transform is de-

fined as

$$P = \mathcal{F}(y),\tag{A.1}$$

where  $\mathcal{F}$  denotes the Fourier transform, and the Fourier axis k represents the characteristic period (or inverse frequency) of variations along the spectrum. Panel c of Figure A.4 shows a mask (green line), denoted as  $\mathcal{M}_k$ , which selects periods with abnormally high power. The mask also includes the first few low-k periods corresponding to the non-constant spectral baseline.

We denote the velocity channels containing real spectral lines that we aim to preserve as  $\mathcal{M}_V$  (in this example, selected as -20 to  $10 \text{ km s}^{-1}$ ). The RFI component, i.e., the comb-like wave  $y_r$ , is iteratively reconstructed as

$$y_r \leftarrow \mathcal{F}^{-1} \left( \mathcal{M}_k \mathcal{F}(y^{\dagger}) \right),$$
 (A.2)

where  $\mathcal{F}^{-1}$  denotes the inverse Fourier transform, mapping the masked subspace defined by  $\mathcal{M}_k$  back to the spectral domain. The intermediate signal is given by

$$y_i^{\dagger} = \begin{cases} y_i & \text{if } i \in \mathcal{M}_V, \\ y_{r,i} & \text{otherwise,} \end{cases}$$
 (A.3)

with *i* the velocity-channel index. In this iterative procedure, the spectral-line channels are excluded when constructing the RFI component, and the RFI signal is modeled from the remaining channels. This approach allows for a clean separation of RFI from the astrophysical signal while preserving the true spectral-line features.

The RFI-removed and spectral-baseline-subtracted spectrum, denoted as  $y^*$ , is obtained as

$$y^* = y - y_r. \tag{A.4}$$

The resultant  $y^*$  for the example RFI-contaminated spectrum is shown in panel d of Figure A.4, and it is in good agreement with its neighboring spectrum. We note, however, that the noise level of  $y^*$  remains higher than that of the neighboring spectrum, and some residual spikes cannot be fully removed. Therefore, special caution is required when incorporating RFI-removed spectra into the final data cube.

In practice, this Fourier-based RFI removal method performs reliably when each contiguous block of the Fourier mask  $\mathcal{M}_k$  contains fewer channels than roughly  $|\mathcal{M}_V|/4$ , where  $|\mathcal{M}_V|$  denotes the number of excluded spectral-line channels. This condition arises because a block of width  $\Delta K$  in Fourier space induces a modulation in the spectral domain with a characteristic period of approximately  $T_{\text{mod}} \sim N\Delta K$ , where N is the total number of spectral channels. If the modulation period exceeds the width of  $\mathcal{M}_V$ , the missing channels do not provide sufficient information to constrain the RFI model accurately, and the reconstruction becomes unreliable.

#### **Appendix B: Foreground emission**

Figure B.1 shows the foreground H<sub>1</sub> emission of the AC-III region. A two-dimensional Gaussian fitting,

$$f = A\left(1 - A_r \exp\left(-\frac{r^2}{2\sigma^2}\right)\right),\tag{B.1}$$

to the foreground (-10 to  $20 \text{ km s}^{-1}$ ) H I moment 0 map yields an absorption dip ratio of  $A_r = 0.18$ . The peak brightness temperature of the brightest background continuum source (at the FAST

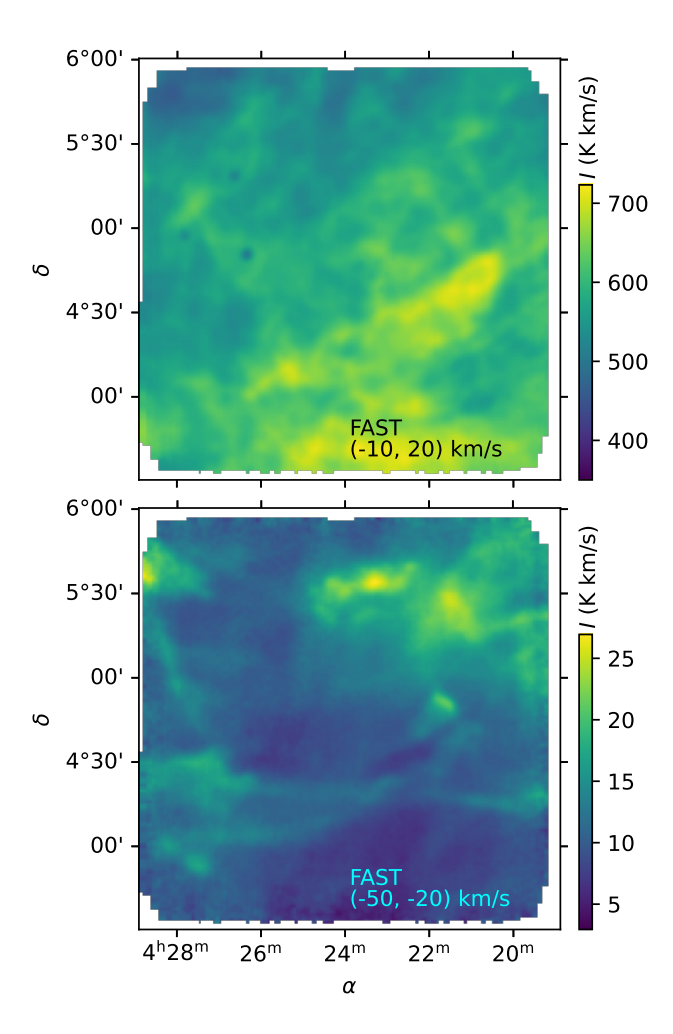


**Fig. B.1.** Foreground H<sub>I</sub> emission in the region of AC-III, integrated over the velocity ranges indicated in the lower right corner of each panel.

resolution) is  $T_c = 16.36$  K (Sect. A.2). Assuming that the foreground H I mainly consists of warm neutral medium (WNM), the spin temperature of the foreground H I is estimated as

$$T_{\rm s,f} \sim \frac{T_c}{A_r} \sim 90 \text{ K},$$
 (B.2)

which is consistent with the typical value of the cold neutral medium (CNM; Heiles & Troland 2003; Kalberla & Kerp 2009). The peak brightness temperature of the foreground H  $\scriptstyle\rm I$  is  $\sim 60$  K, corresponding to an optical depth of unity. Note that the HVC H  $\scriptstyle\rm I$  emission is unaffected because of the large velocity separation.

No absorption signatures against the background continuum sources are detected for HVC AC-III. The signal-to-noise ratio of the moment 0 map of HVC AC-III at the position of the brightest continuum source is 135, yielding a  $3\sigma$  confidence lower limit on the H I spin temperature of

$$T_{s, HVC} > 45 \times T_c \sim 700 \text{ K},$$
 (B.3)

which is consistent with the conclusion that AC-III mainly consists of WNM.